# CONFORMATIONAL ANALYSIS OF ASTROCHEMICALLY RELEVANT MOLECULES USING ROTATIONAL SPECTROSCOPY

**AADYA CHAUDHARY**

A THESIS SUBMITTED TO THE FACULTY OF GRADUATE STUDIES IN PARTIAL FULFILLMENT OF THE REQUIREMENTS FOR THE DEGREE OF MASTER OF SCIENCE

GRADUATE PROGRAM IN CHEMISTRY
YORK UNIVERSITY
TORONTO, ONTARIO

December 2025

# Abstract

Rotational spectroscopy was employed to investigate the conformational preferences and internal dynamics of two sulfur-containing organic molecules, allyl phenyl sulfide (APS) and 2-methylthioethylamine (2-mtea). Supersonic jet-cooled Fourier transform microwave (FTMW) spectroscopy, supported by quantum chemical calculations, enabled the identification and characterization of low-energy conformers for both systems. The analysis of hyperfine structure due to the $^{14}N$ nuclear quadrupole coupling and internal methyl rotation in 2-mtea provided detailed insights into the electronic and structural effects of sulfur and nitrogen substitution. Natural bond orbital (NBO) analysis revealed key orbital interactions between the lone pairs of sulfur and nitrogen and the various organic side chains that govern conformational stability. These findings contribute to a deeper understanding of the conformational behavior of S and N containing organic molecules, which are of growing interest in astrochemical contexts.

## Acknowledgements

I want to thank my supervisor, Dr. Jennifer van Wijngaarden, for being an incredibly patient and encouraging mentor throughout my program. Under her guidance, I have learned to be a researcher and gained wisdom on the continuous hard work that goes into being a scientist. Her passion and commitment towards her work is beyond inspiring and has been a constant source of motivation over the past two years.

I also want to thank my advisory committee, Dr. Rene Fournier and Dr. Cora Young, for their kindness and enthusiasm for my research.

I would like to thank my current group members; Dylan James, Sophia Worthington-Kirsch and Polity Chheang for their support and the many useful and interesting discussions.

My deepest gratitude goes to my family for their unconditional love and support throughout my academic pursuits, without whom I could not have done this.

And finally, many thanks to the Faculty of Graduate Studies, the Faculty of Science and the Department of Chemistry for the financial support provided through scholarships, and the York University Graduate Fellowship.

# Table of Contents

# List of Tables

# List of Figures

# Chapter 1. Introduction

## 1.1. Overview of interstellar chemistry

Astrochemistry is the field that bridges astronomy, chemistry, and physics to study how atoms and molecules form, survive, and evolve in space under the extreme environments found in the interstellar medium (ISM), circumstellar envelopes, and protostellar regions.[1] The ISM presents unique conditions: densities which are often many orders of magnitude lower than in terrestrial laboratories (down to $10^5$–$10^6$ particles $cm^{-3}$)[2], temperatures ranging from ~10 K in dark, cold molecular clouds to several hundred Kelvin in warmer star-forming regions, strong UV radiation fields, cosmic rays, and dust grains that can catalyze surface reactions.[3-4] Under these conditions, reaction pathways and molecular lifetimes differ greatly from Earth-based chemistry, making observational detection of molecules essential for constraining chemical networks and physical conditions.

Interstellar chemistry reveals a rich molecular diversity in the Universe, from the simplest diatomic species to relatively large, complex organic molecules (COMs),[5] which are – by definition – molecules containing more than 5 atoms and including at least one carbon atom. To date, over two hundred molecular species have been detected in interstellar, circumstellar and extragalactic environments, constructed from about 19 different chemical elements. These species vary from simple atoms and radicals (e.g., CN, CH) to small organics (e.g., formaldehyde, ammonia, methanol) and further into molecules with functional groups such as aldehydes, alcohols, acids and amines.[6] Particularly in cold dark clouds like TMC-1, species with long carbon-chain backbones and cumulene carbenes, which are polar, linear carbon chains with the formula $H_2C_n$ that feature consecutive double bonds and have two non-bonded electrons on a terminal carbon atom,

are abundant, revealing that unsaturated linear molecules are more common in low-temperature regions than fully saturated or large cyclic ones.[7] More recently, increasingly complex molecules have been identified: for example, methyl formate ($HCOOCH_3$), vinyl alcohol ($C_2H_3OH$), propenal ($C_2H_3CHO$) and dimethyl ether ($CH_3OCH_3$) have been detected in cold, starless cores,[8] showing that complexity is not restricted to hot cores. On the aromatic and polycyclic side, recent detections of polycyclic aromatic hydrocarbons (PAHs) and substituted PAHs such as cyanopyrene mark another step in chemical complexity, hinting at carbon-rich chemistry that may contribute substantially to the carbon budget of molecular clouds.[9]

## 1.2. Astrochemistry and the role of rotational spectroscopy

Detection of atoms and molecules in space relies predominantly on remote spectroscopic techniques. Atoms are typically identified through their electronic transitions observable in the ultraviolet (UV), visible, or near-infrared regions of the spectrum, while molecules are most often detected via their quantized rotational and vibrational transitions.[5] Rotational transitions, which arise from quantized changes in a molecule's angular momentum, occur in the radio, microwave, millimeter and submillimeter frequency regimes.[11] These regions of the spectrum are particularly informative for astrochemical studies, as many molecules in the cold ISM reside primarily in their lowest rotational states. Under these conditions, vibrational and electronic energy levels remain largely unpopulated, making rotational spectroscopy a uniquely sensitive tool for probing molecular composition and structure.[12-13] Because rotational spectra are highly molecule-specific, each species exhibits a characteristic set of discrete transitions that act as "fingerprints" in astronomical observations.[6] This serves as one of the most fundamental

tools for identifying new interstellar molecules and understanding the physical and chemical environments of diverse astronomical sources from cold dark clouds to star-forming regions and protoplanetary disks.[14]

Laboratory spectroscopy plays a foundational role in enabling these detections. High-precision measurements of rotational spectra yield rest frequencies, dipole moments, rotational constants, centrifugal distortion constants, and hyperfine structures related to charge distribution or internal re-arrangements. This data is essential for unambiguously matching astronomical spectral lines to molecular carriers. For example, the recent detection of 2-methoxyethanol in NGC 6334I was made possible only after its laboratory spectrum had been recorded over a broad frequency range (~8-500 GHz), enabling identification of multiple unblended rotational transitions in ALMA observations.[15] Similarly, propargylimine has been detected in space following laboratory millimeter-wave spectral work combined with quantum chemical predictions to guide both the line assignment and astronomical search.[16]

The synergy between laboratory work, quantum chemistry, and astronomical observations is central: quantum chemical (*ab initio*) computations support prediction of rotational constants and dipole moments, help fill gaps where laboratory data is lacking, and guide instrument tuning and surveys. Chemical models, mediated by databases such as the UMIST Database for Astrochemistry[17], depend on both observed abundances and reaction-rate data (from theory or experiment) to simulate molecular formation, destruction, and abundances in various astrophysical environments.[18]

## 1.3. Astrochemistry of sulfur and nitrogen

Sulfur and nitrogen bearing molecules are among the most chemically and astrobiologically significant species in the ISM. Both elements are moderately abundant and participate in a wide range of chemical networks that span from cold dark clouds to hot cores, comets, and protoplanetary disks. They act not only as tracers of physical conditions in the ISM but also as molecular bridges toward chemical complexity and potential prebiotic chemistry. Both elements participate in rich and varied reaction networks that give rise to families of molecules such as $H_2S$, $SO_2$, CS, HCN, $NH_3$, and more complex species like thioethers, amines, and amides, which have been detected in cold molecular clouds and hot cores.[8,10] The combination of nitrogen's high electronegativity and sulfur's chemical flexibility enables the formation of diverse functionalities such as thiols, sulfides, imines, and amines, that can serve as building blocks for larger organic molecules on grain surfaces or in warm gas-phase environments. In astrochemistry, such heteroatom-containing organics are thought to represent transitional species between simple interstellar precursors (e.g., $H_2CS$, $CH_3SH$, $NH_2CHO$) and the more complex, aromatic or aliphatic compounds detected in protostellar and cometary material.[5]

The identification and characterization of these molecules rely heavily on rotational spectroscopy.[6,13] Because sulfur and nitrogen often introduce significant dipole moments and anisotropic electron distributions, their substitution within a carbon framework leads to distinctive rotational spectra and, in some cases, nuclear quadrupolar hyperfine structure from nuclei such as the $^{14}N$ (spin (I) = 1).[13] Theoretical calculations and laboratory spectra of small thioethers or alkylamines, for instance, enable the

construction of accurate spectral catalogs that can be compared with data from facilities such as ALMA or the Green Bank Telescope.[6,15] As astrochemistry continues to expand, the integration of rotational spectroscopy with quantum chemistry, laboratory astrophysics, and astronomical observation remains central to decoding the molecular universe.

This thesis explores two related projects focused on the conformational behavior of sulfur-containing molecules. The first involves allyl phenyl sulfide (APS) and allyl phenyl ether (APE), which serve as model systems to investigate how chalcogen substitution (sulfur vs. oxygen) influences conformational preferences. The second project centers on 2-methylthioethylamine (2-mtea), a molecule of astrochemical interest due to its flexible backbone, internal methyl rotation, and the presence of a nitrogen nucleus that gives rise to hyperfine structure. Together, these studies aim to probe the effects of functional group substitution and internal motion on molecular structure and spectroscopic signatures.

## 1.4. References


1. Shematovich, V. I. Formation of Complex Chemical Species in Astrochemistry (a Review). *Sol. Syst. Res.* **2012,** *46* (6), 391-407.
2. Di Francesco, J.; Evans II, N. J.; Caselli, P.; Myers, P. C.; Shirley, Y.; Aikawa, Y.; Tafalla, M. *An Observational Perspective of Low-Mass Dense Cores I: Internal Physical and Chemical Properties*. Univerisity of Arizona Press: 2006; p 17.
3. Chevance, M.; Kruijssen, J. M. D.; Vazquez-Semadeni, E.; Nakamura, F.; Klessen, R.; Ballesteros-Paredes, J.; Inutsuka, S. ichiro; Adamo, A.; Hennebelle, P. The *Molecular Cloud Lifecycle*. Space Sci. Rev. 2020, 216 (4), 1–42.
4. Gerin, M. *The Molecular Universe. In Astrochemistry and Astrobiology*; Smith, I. W. M., Cockell, C. S., Leach, S., Eds.; Springer Berlin Heidelberg: Berlin, Heidelberg, 2013; pp 35–72.
5. Herbst, E.; van Dishoeck, E. F. Complex Organic Interstellar Molecules. *Annu. Rev. Astron. Astrophys.* **2009**, *47*, 427–480.
6. McGuire, B. A. 2021 Census of Interstellar, Circumstellar, Extragalactic, Protoplanetary Disk, and Exoplanetary Molecules. Astrophys. J. Suppl. Ser. 2022, 259 (2), 30.
7. Taniguchi, K.; Gorai, P.; Tan, J. C. Carbon-Chain Chemistry in the Interstellar Medium. *Astrophys. Space Sci.* **2024**, *369*, 34.
8. Agúndez, M.; Marcelino, N.; Tercero, B.; Cabezas, C.; de Vicente, P.; Cernicharo, J. O-Bearing Complex Organic Molecules at the Cyanopolyyne Peak of TMC-1: Detection of $C_2H_3CHO$, $C_2H_3OH$, $HCOOCH_3$, and $CH_3OCH_3$. *Astrophys. Space Sci.* **2021**, *649*, L4.

9. Wenzel, G.; Cooke, I. R.; Changala, P. B.; et al. Detection of Interstellar 1-Cyanopyrene: A Four-Ring Polycyclic Aromatic Hydrocarbon. *Science* **2024**, *386* (6723), 810–813.
10. Laas, J. C.; Caselli, P. Sulfur Chemistry in Prestellar Cores: The Influence of Accretion, Desorption, and Diffusion Barriers on Sulfur-Bearing Species. *Astrophys. J.* **2019**, *876* (2), 101.
11. Wilson, T. L.; Rohlfs, K.; Hüttemeister, S. *Tools of Radio Astronomy*; Springer: Berlin, 2013.
12. Townes, C. H.; Schawlow, A. L. *Microwave Spectroscopy*; Dover Publications: New York, 1975.
13. Gordy, W.; Cook, R. L. *Microwave Molecular Spectra*, 3rd ed.; Wiley: New York, 1984.
14. Puzzarini, C.; Tasinato, N.; Barone, V. The Challenge of Small Molecules Containing Heavy Elements: High-Level Quantum Chemical Predictions for Rotational Spectroscopy. *Front. Astron. Space Sci.* **2022**, *9*, 787567.
15. Fried, Z. T. P.; El-Abd, S. J.; Hays, B. M.; Wenzel, G.; Byrne, A. N.; Margulès, L.; Motiyenko, R. A.; Shipman, S. T.; Horne, M. P.; Jørgensen, J. K.; Brogan, C. L.; Hunter, T. R.; Remijan, A. J.; Lipnicky, A.; Loomis, R. A.; McGuire, B. A. Rotational Spectrum and First Interstellar Detection of 2-Methoxyethanol Using ALMA Observations of NGC 6334I. *Astrophys. J. Lett.* **2024**, *963*, L12.
16. Bizzocchi, L.; Giuliano, B. M.; Prudenzano, D.; et al. Rotational Spectrum and First Detection in Space of the HCN Dimer: Propargylimine. *J. Chem. Phys.* **2020**, *152*, 184303.
17. Millar, T. J.; Walsh, C.; Van de Sande, M.; Markwick, A. J. *The UMIST Database for Astrochemistry 2022* (UDfA2024). UDfA Database Release (via UMIST Database for Astrochemistry, UK). 2024.

18. Taniguchi, K.; Gorai, P.; Tan, J. C. Carbon-Chain Chemistry in the Interstellar Medium. *Astrophys. Space Sci.* **2024**, *369*, 34.
19. Pickett, H. M.; Poynter, R. L.; Cohen, E. A.; Delitsky, M. L.; Pearson, J. C.; Müller, H. S. P. Submillimeter, Millimeter, and Microwave Spectral Line Catalog. *J. Quant. Spectrosc. Radiat. Transfer* **1998**, *60* (5), 883–890.

# Chapter 2. Fourier transform microwave spectroscopy

## 2.1. Overview

Rotational microwave spectroscopy is a highly sensitive technique that probes the rotational transitions of molecules in the microwave or centimeter-wave region of the electromagnetic spectrum. Only molecules with a permanent electric dipole moment produce pure rotational spectra, but for these systems, the method provides exceptionally precise rotational and centrifugal distortion constants. Because rotational constants are directly related to the molecular moments of inertia for rotation, they serve as a detailed fingerprint of molecular geometry. This allows researchers to distinguish between different conformers, identify isotopologues, and even assess the influence of internal motions, such as hindered rotations, which manifest as characteristic splitting of the transitions in the rotational spectrum.[2-5]

Rotational spectroscopy also provides valuable insight into intramolecular forces and electronic structure. Measurements and analysis of nuclear quadrupole splitting shed light on electronic distributions which influence, for example, internal barriers to motion. Weak non-covalent interactions, such as hydrogen bonding and van der Waals forces, can also be revealed in this way. Importantly, rotational spectra offer a direct and accurate comparison to quantum chemical predictions, making them an essential benchmark for validating computational results. Furthermore, isotopic substitution experiments enable structure determination with high precision. In the following section, a brief description of the background theory of microwave spectroscopy is described referring to fundamental spectroscopy textbooks.[3-7]

## 2.2. Microwave spectroscopy theory

### 2.2.1. Introduction

Rotational spectroscopy exploits the unique moments of inertia of molecules, which are determined by the distribution of atomic masses and their relative positions in the molecule. The moments of inertia are calculated using the equation[3-5]:

$$I_R = \sum m_i r_i^2$$

Here, $m_i$ represents the mass of the i$^{th}$ atom, and $r_i$ is the distance of the atom from the axis of rotation, with R = a, b, c denoting the principal inertial axes of the molecule. From this equation, it is clear that the moments of inertia are specific to both the atom types and their arrangement in space, making them highly sensitive to the molecular geometry in a given conformation.

### 2.2.2. Rigid rotor approximation

Microwave or rotational transitions occur when electromagnetic radiation in the microwave region of the spectrum matches the characteristic separation of rotational energy levels of a molecule. To describe rotational energy levels, the simplest starting point is the rigid rotor model, which assumes that the molecule rotates as a rigid body with fixed bond lengths and angles. For a diatomic molecule, the Hamiltonian of a rigid rotor is expressed as:

$$\hat{\mathrm{H}} = \frac{\hat{J}^2}{2I}$$

Where $\hat{J}^2$ is the total angular moment operator and I is the moment of inertia for rotation about an inertial axis perpendicular to the bond axis, also defined as

$$I = \mu r^2 \; where \; \mu = \frac{m_1 m_2}{(m_1 + m_2)}$$

After solving the Schrödinger equation, we can find the eigen values corresponding to quantized rotational energy levels[3-5]:

$$E(J) = BJ(J+1)$$

where J is the rotational quantum number (J=0,1,2,...) and

$$B = \frac{h}{8\pi^2 I}$$

is the rotational constant in SI unit of Hz . Transitions between adjacent rotational levels in diatomic molecules follow the selection rule $\Delta J = \pm 1$.[3-6] The spacing of levels is therefore inversely proportional to the moment of inertia. Small, light molecules such as HF (short bond length, small I) exhibit widely spaced transitions, whereas heavier molecules such as ICl (large I) produce closely spaced spectra in the frequency domain.[6,8] This simple diatomic case provides the conceptual framework for more complex rotors. In polyatomic molecules, instead of a single value of I, three principal moments of inertia ($I_a$, $I_b$ and $I_c$) can be defined relative to the three principal axes of rotation. These moments determine the type of rotor (linear, symmetric, or asymmetric) and form the basis for the Hamiltonians used in high-resolution rotational spectroscopy.

### 2.2.3. Linear tops

For linear molecules (e.g., $CO_2$, HCN, or acetylene), two of the three principal moments of inertia are equivalent ($I_a << I_b = I_c$). The rotational Hamiltonian is formally identical to the diatomic case, with energy levels:

$$E(J) = BJ(J+1)$$

and rotational transitions governed by the selection rule $\Delta J = \pm 1$. An example is carbonyl sulfide (OCS), a linear triatomic molecule with a strong dipole moment, widely studied in astrophysics and laboratory spectroscopy. Such spectra appear as evenly spaced lines, and deviations from the rigid rotor approximation arise from centrifugal distortion, which can be accounted for by including correction terms proportional to $DJ^2 (J+1)^2$, where D is the centrifugal distortion constant.[3-7] More details will be provided on centrifugal distortion in the upcoming sections.

### 2.2.4. Symmetric tops

In symmetric top molecules, two of the principal moments of inertia are equal, while the third is distinct. Molecules such as $CH_3Cl$ (prolate symmetric top) and benzene (oblate symmetric top) are relevant examples. The rotational Hamiltonian in this case is:

$$H = AJ_a^2 + B\left(J_b^2 + J_c^2\right),$$

for a prolate top ($A \neq B = C$), or

$$H = CJ_c^2 + B\left(J_b^2 + J_a^2\right)$$

for an oblate top ($C \neq A = B$).

The eigenvalues are then expressed as:

$$E(J,K) = BJ(J+1) + (A-B)K^2 \text{ for prolate tops,}$$

$$E(J,K) = BJ(J+1) + (C-B)K^2 \text{ for oblate tops}$$

where J is the total angular momentum quantum number, and K is its projection along the unique symmetry axis. Transitions follow the selection rules $\Delta J = \pm 1$ and $\Delta K = 0$.[3-7] As mentioned in the above section, when the restriction of rigidity is removed, symmetric tops are affected by centrifugal distortion as they rotate. Three distortion constants $D_J$, $D_K$, $D_{JK}$ are included to model the effect.

### 2.2.5. Asymmetric tops

Most polyatomic molecules, including those of chemical and biological interest, are neither linear nor symmetric. Such molecules are described as asymmetric rotors. Here, all three principal moments of inertia are distinct ($I_a \neq I_b \neq I_c$). The rotational Hamiltonian for an asymmetric top can be expressed as:

$$H = AJ_a^2 + BJ_b^2 + CJ_c^2$$

with $A = \frac{h}{8\pi^2 c I_a}$, $B = \frac{h}{8\pi^2 c I_b}$ and $C = \frac{h}{8\pi^2 c I_c}$.[3-5] Unlike symmetric tops, there is no analytical solution to the Schrödinger equation and hence there is no exact conserved projection quantum number and symmetric-top wavefunctions are used to derive approximate energies. The rotational

states are then labeled using pseudo-quantum numbers $K_a$ and $K_c$ which are not strictly good quantum numbers but correlate to the prolate ($K_a$) oblate ($K_c$) limits.

Ray's asymmetry parameter, κ, provides a way to describe how close a molecule is to the symmetric-top limits:

$$\kappa = \frac{2B-A-C}{A-C}$$

- κ = -1 for prolate symmetric top
- κ = +1 for oblate symmetric top
- -1 < κ < +1 for asymmetric top

For any type of molecule, a transition is only possible if it corresponds to a non-zero electric dipole moment along one of the principal axes, and the selection rule ΔJ = 0, ±1 must be satisfied. Furthermore, due to the three principal axes, each molecule may have three types of transitions, a schematic of which is shown in figure 2.1. Each transition has its own selection rules, provided there is a nonzero dipole component along the principal inertial axes:

1. **a-type transitions**: $\mu_a \neq 0$; $\Delta K_a = \pm 2k$ and $\Delta K_c = \pm 2k + 1$, for any integer k. The strongest transitions occur at k = 0.
2. **b-type transitions**: $\mu_b \neq 0$; $\Delta K_a = \pm 2k + 1$ and $\Delta K_c = \pm 2k + 1$, for any integer k.
3. **c-type transitions**: $\mu_c \neq 0$; $\Delta K_a = \pm 2k + 1$ and $\Delta K_c = \pm 2\ k$, for any integer k.

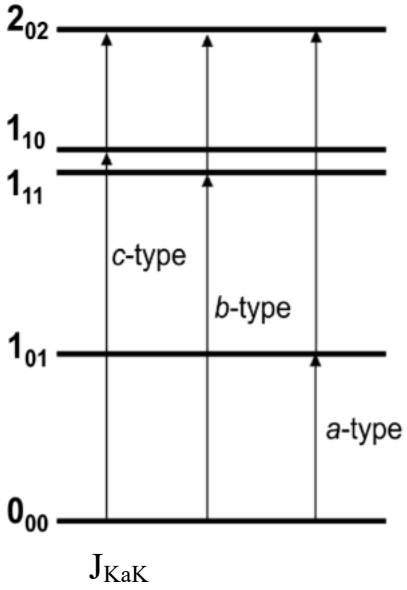


*Figure 2.1: Rotational energy level diagram showing a-type, b-type, and c-type transitions*

Asymmetric tops dominate in chemical and biological systems. The water molecule ($H_2O$)[16], for instance, provides the prototypical example of an asymmetric top with strong astrophysical relevance, while formaldehyde ($H_2CO$)[17] has historically served as a benchmark for microwave spectroscopic techniques. Molecules such as methylamine ($CH_3NH_2$)[19] and methyl cyanide ($CH_3CN$)[18] exhibit high levels of complexity in their spectra, including internal rotation splittings and nuclear quadrupole hyperfine interactions, which makes asymmetric top molecules particularly rich subjects for both experimental and computational analysis.

### 2.2.6. Centrifugal distortion

One of the assumptions of the rigid rotor model is that the geometry of a molecule remains unchanged during rotation. This model is most acceptable when considering only the lower rotational energy levels but as the rotational energy increases, molecules are no longer rigid and the effects of the centrifugal forces acting on the atoms as the molecule rotates become more pronounced. These forces distort the internuclear positions which affects the bond lengths and angles, resulting in a decrease in the energy difference between the rotational levels. In order to accurately model the rotational spectrum, a correction term, often represented by a "D" constant, is added to the rotational energy equation to account for centrifugal distortion.[3-5]

The simplest way to illustrate centrifugal distortion is through the diatomic rigid rotor. The rigid rotor energy levels are given by[3-7]:

$$E(J) = BJ(J+1)$$

where $B = \frac{h}{8\pi^2 cI}$ is the rotational constant, J is the rotational quantum number, and I is the moment of inertia. When centrifugal distortion is considered, a quartic correction term is introduced:

$$E(J) = BJ(J+1) + DJ^2 (J+1)^2$$

where D is the centrifugal distortion constant. The second term reduces the spacing between adjacent rotational levels at high J, reflecting the bond stretching under centrifugal force.

For polyatomic molecules, centrifugal distortion is incorporated into the effective rotational Hamiltonian by adding up to five quartic centrifugal distortion terms, called $\Delta_J$, $\Delta_{JK}$, $\Delta_K$, $\delta_J$, and $\delta_K$ in Watson's A-reduced representation[7], to describe these effects although higher order terms (sextic and beyond) are needed for highly distortable rotors. These constants are determined experimentally by fitting observed rotational spectra and provide quantitative information about molecular flexibility. For example, compact rigid molecules such as water or formaldehyde have relatively small distortion constants, while floppy molecules such as large ethers, amines, or hydrogen-bonded clusters may require inclusion of sextic or even higher-order terms for accurate spectral fitting depending on how many high quantum number states are accessed. Thus, centrifugal distortion not only refines the accuracy of the Hamiltonian used in rotational spectroscopy but also serves as a diagnostic of molecular structure and dynamics.

Beyond rigid-body rotation, microwave spectra provide insight into internal motions (e.g., methyl internal rotation, large-amplitude torsions), as well as hyperfine structure from nuclei with quadrupole moments (e.g., $^{14}$N, $^{35}$Cl). For asymmetric molecules, these effects often lead to splitting patterns that are highly diagnostic of structure and bonding.

## 2.3. Nuclear quadrupolar interaction

Certain molecules contain atoms that possess a nuclear spin greater than ½, such as a $^{14}$N atom with a spin of 1. The rotational spectra of these molecules are consequently more complex, exhibiting splitting patterns referred to as nuclear quadrupole hyperfine structure.[12-13] This phenomenon arises from the interaction of the non-zero nuclear quadrupole moment Q with the nonspherical electric field gradient (EFG) at the nucleus, which is generated by the surrounding electronic charge distribution. The magnitude and symmetry of this electric field gradient are

determined by the local electronic environment, making nuclear quadrupole hyperfine splittings highly sensitive probes of molecular geometry and bonding.

For molecules containing a single quadrupolar nucleus, the energy levels are labelled as follows. The nuclear spin vector I couples to the rotational angular momentum vector J of the molecule, resulting in a total angular momentum F = J+I. The total angular momentum quantum number F can take values from |J−I| to J+I in integer steps:

$$J + I, J + I - 1, J + I - 2, \ldots, | J - I |$$

Consequently, each rotational energy level $J_{K_aK_c}$ is split into multiple F levels, denoted as $J_{k_ak_cF}$. The energy shifts due to the quadrupolar interaction are commonly described using the nuclear quadrupole Hamiltonian. In practice, for asymmetric top molecules, this leads to observable splitting patterns in the microwave spectrum, the analysis of which allows extraction of quadrupole coupling constants ($\chi_{aa}$ ,$\chi_{bb}$ ,$\chi_{cc}$ ), providing detailed information on the electronic environment around the nucleus. The selection rules governing transitions between hyperfine levels are $\Delta F = 0, \pm 1$, in addition to the usual rotational selection rules. The resulting spectral lines are therefore split into multiplets, with the number and relative intensities of the components depending on the nuclear spin, rotational quantum numbers, and symmetry of the molecule. These splittings are often well-resolved in high-resolution microwave spectroscopy and serve as a powerful tool for structural characterization and assignment of molecular conformers.

## 2.4. Three-fold methyl rotation

In molecules containing methyl groups, the threefold symmetry of the $CH_3$ unit gives rise to three equivalent minima if one considers internal rotation about the bond connecting the methyl carbon to the molecular framework.[9-11] This torsional motion is hindered by a potential energy barrier, most often approximated by a cosine series expansion, with the leading term being the threefold contribution:

$$V(\alpha) = \frac{1}{2}V_3(1 - \cos 3\,\alpha)$$

where α is the internal rotation angle and $V_3$ is the barrier height to internal rotation. The magnitude of $V_3$ depends strongly on the local chemical environment; for example, methyl groups bound to electronegative atoms (e.g., O–$CH_3$) typically experience lower barriers due to electron delocalization, whereas larger alkanes and sterically hindered sites can result in higher barriers. Determining $V_3$ is central to understanding torsional dynamics and the degree of coupling between internal rotation and the overall molecular rotation.

When the barrier is finite, the internal rotor is neither completely free nor completely fixed. Instead, the methyl torsional motion couples with the rigid-body rotation of the molecule. This coupling manifests in the rotational spectrum as characteristic splittings of transitions. In the high-barrier limit ($V_3 \rightarrow \infty$), the methyl group is effectively locked in place, and the spectrum is described by a rigid rotor Hamiltonian with no torsional effects. In the opposite extreme, a very low $V_3$ approximates a free rotor, leading to widely separated torsional energy levels. Most molecules of spectroscopic interest fall between these limits, where the finite barrier produces resolvable splittings in the microwave spectrum that can be analyzed to extract torsional parameters.

*A/E splitting patterns*

The spectral signature of methyl internal rotation is the so-called A/E splitting. This arises from the symmetry of the $CH_3$ top, which belongs to the $C_{3v}$ point group. The torsional wavefunctions transform according to the totally symmetric A representation or the doubly degenerate E representation. As a result, each rotational transition of the parent molecule can split into two components, corresponding to the A and E torsional states. This can be seen in figure 2.2 where conformer 1 of Allyl ethyl ether is split into two distinct A and E states.[9] The magnitude of this splitting depends sensitively on the barrier height: at low $V_3$, the splitting can be on the order of tens to hundreds of MHz, while at high $V_3$ the splittings may reduce to only a few kHz, sometimes below the resolution of conventional Fourier transform microwave spectrometers.

Observation of A/E splitting patterns thus provides a powerful diagnostic for probing internal rotation. Analysis typically includes fitting the observed A/E splittings with software programs like XIAM[14] based on the combined axis method, which directly fits the $V_3$ barrier to internal rotation, the angles between the internal rotation axis and the principal axes and the moment of inertia of the internal top.

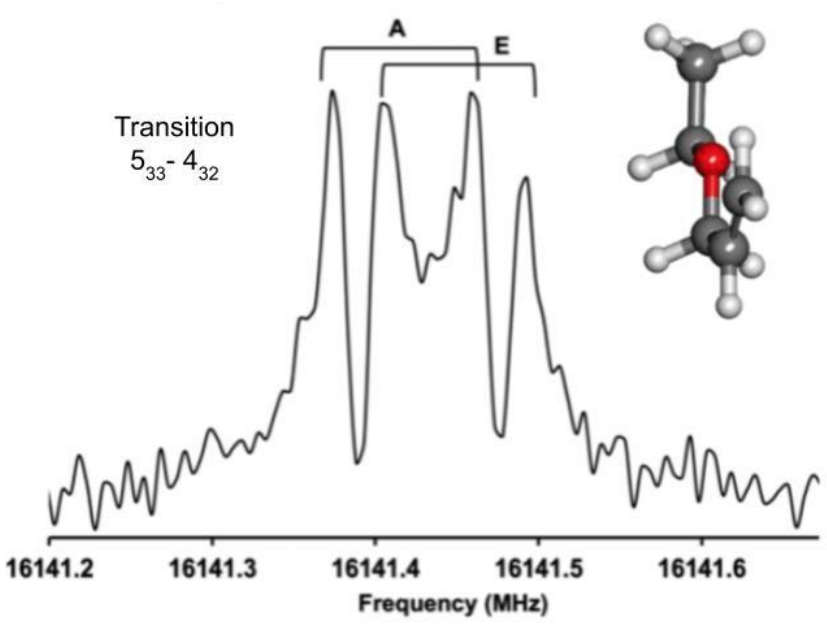


*Figure 2.2: Spectrum of the $5_{33}$-$4_{32}$ transition of conformer 1 of AEE[9] on the BF-FTMW showing A/E splitting in addition to the Doppler splitting that is an artefact of the instrument.*

The study of methyl internal rotation is not only important for accurately fitting and predicting rotational spectra, but also for gaining chemical insight. The extracted $V_3$ barriers reflect steric hindrance, electronic effects, and intermolecular interactions, while the A/E splitting patterns provide direct evidence of large-amplitude motions within the molecule. Such analyses have been applied to a wide range of systems, from simple molecules like methanol and acetaldehyde to larger biomolecular building blocks[20] where internal rotation plays a role in conformational flexibility. In astrophysics, identifying A/E splittings in interstellar spectra has proven essential for confirming the presence of methyl-containing molecules in the interstellar medium, emphasizing the wide-ranging significance of these effects.[21-23]

## 2.5. References


1. McGuire, B. A. (2022). 2021 Census of Interstellar, Circumstellar, Extragalactic, Protoplanetary Disk, and Exoplanetary Molecules. *The Astrophysical Journal Supplement Series*, 259(2), 30.
2. Bauder, A. Fundamentals of Rotational Spectroscopy. In *Encyclopedia of Spectroscopy and Spectrometry*; Lindon, J. C., Tranter, G. E., Holmes, J. D., Eds.; Elsevier: Oxford, 2011
3. Bernath, P. F. *Spectra of atoms and molecules*. Oxford university press: 2015.
4. Hollas, J. M. *Modern spectroscopy*. John Wiley & Sons: 2004.
5. Gordy, W.; Cook, R. L. *Microwave Molecular Spectra*. Wiley: 1984.
6. Townes, C. H.; Schawlow, A. L. *Microwave Spectroscopy*; Dover: New York, 1975
7. Watson, J. K. G. "Determination of Centrifugal Distortion Coefficients of Asymmetric-Top Molecules." *J. Chem. Phys.* **1967**, *46*, 1935–1949.
8. Brown, J. M.; Carrington, A. *Rotational Spectroscopy of Diatomic Molecules*; Cambridge University Press: Cambridge, 2003.
9. Poonia, T.; van Wijngaarden, J. Exploring the Distinct Conformational Preferences of Allyl Ethyl Ether and Allyl Ethyl Sulfide Using Rotational Spectroscopy and Computational Chemistry. *J. Chem. Phys.* **2023**, *158* (22), 224301.
10. Lister, D. G.; MacDonald, J. N.; Owen, N. L. Internal Rotation and Inversion; Academic Press Inc.: London, 1978.
11. Kleiner, I. Asymmetric-Top Molecules Containing One Methyl-like Internal Rotor: Methods and Codes for Fitting and Predicting Spectra. J. Mol. Spectrosc. 2010, 260 (1), 1– 18.
12. Kleiner, I. Spectroscopy of Interstellar Internal Rotors: An Important Tool for Investigating Interstellar Chemistry. ACS Earth Sp. Chem. 2019, 3 (9), 1812–1842.

13. Hansen, N.; Mäder, H.; Bruhn, T. A Molecular Beam Fourier Transform Microwave Study of 0-Tolunitrile: $^{14}$N Nuclear Quadrupole Coupling and Methyl Internal Rotation Effects. Mol. Phys. 1999, 97 (4), 587–595.
14. Surin, L.; Tarabukin, I.; Pérez, C.; Schnell, M. Microwave Spectra and Nuclear Quadrupole Structure of the $NH_3$–$N_2$ van der Waals Complex and Its Deuterated Isotopologues. *J. Chem. Phys.* **2018**, *149* (22), 224305.
15. Woods, R. A general program for the calculation of internal rotation splittings in microwave spectroscopy. J. Mol. Spectrosc. 1966, 21, 4–24.
16. Carleer, M. R.; Tennyson, J.; Polyansky, O. L.; et al. *IUPAC Critical Evaluation of the Rotational–Vibrational Spectra of Water.* J. Quant. Spectrosc. Radiat. Transfer **2009**, *110*, 573–596.
17. Brünken, S.; Müller, H. S. P.; Lewen, F.; Winnewisser, G. *High Accuracy Measurements on the Ground State Rotational Spectrum of Formaldehyde ($H_2CO$) up to 2 THz.* Phys. Chem. Chem. Phys. **2003**, *5*, 1515–1518.
18. Demaison, J.; Boucher, D.; Dubrulle, A**.** Hyperfine Structure in the Microwave Spectrum of Methyl Cyanide. *J. Mol. Spectrosc.* **1979**, *78* (2), 219–226.
19. lyushin, V. V.; Kisiel, Z.; Pszczółkowski, L.; Mäder, H.; Winnewisser, M. The Ground-State Rotational Spectrum of Methylamine, $CH_3NH_2$, from 8 to 500 GHz. *J. Mol. Spectrosc.* **2005**, *234* (2), 132–143.
20. Anggara, K.; et al. Exploring the Molecular Conformation Space by Soft Molecule Design. *J. Am. Chem. Soc.* **2020**, *142* (45), 19356–19364.
21. Belloche, A.; et al. Rotational Spectroscopy, Tentative Interstellar Detection, and Chemical Modeling of N-Methylformamide ($CH_3NHCHO$). *Astron. Astrophys.* **2017**, *602*, A108.
22. Loomis, R. A.; et al. The Detection of Interstellar Ethanimine ($CH_3CHNH$) from the Green Bank Telescope PRIMOS Survey. *Astrophys. J.* **2013**, *767*, L17.

23. Halfen, D. T.; et al. Interstellar Detection of Methyl Isocyanate $CH_3NCO$ in Sgr B2(N): A Link from Molecular Clouds to Comets. *Astrophys. J.* **2015**, *808*, 139.

# Chapter 3. Microwave spectroscopy experimental setup

## 3.1. Overview

The general approach to investigating molecules through rotational spectroscopy follows a standard process. First, a molecule is chosen based on its chemical characteristics and obtained from a commercial source. Simultaneously, quantum chemical calculations are performed to identify the stable conformers and estimate their spectroscopic parameters prior to measurement. After the sample arrives, a chirped pulse Fourier transform microwave (cp-FTMW) spectrometer is used to conduct an initial survey scan, utilizing the predicted values for the molecule's rotational constants to simulate the spectral pattern. This scan is then analyzed to refine the rotational frequency estimates by comparing this simulated spectrum to the newly obtained experimental spectrum and assigning each rotational transition based on patterns of families of quantum numbers to obtain preliminary rotational constants from a least squares fit. Individual rotational transitions are next measured using a Balle-Flygare Fourier transform microwave (bf-FTMW) spectrometer which yields more precise line positions and can identify any line splitting resulting from the internal re-arrangements of the molecule or the presence of quadrupolar nuclei. Finally, the sets of individual transition frequencies are fitted to extract accurate spectroscopic parameters.

In the present study, rotational spectra of various molecules were recorded using both instruments mentioned above, a broadband cp-FTMW spectrometer and a narrowband bf-FTMW spectrometer. These complementary techniques allow for both rapid broadband spectral acquisition across wide frequency ranges and also high-resolution measurements of individual transitions. Experimental liquid samples were introduced into the molecular beam apparatus using helium, argon or neon as the carrier gas at a pressure of 1-5 atm. The gas mixtures were expanded into the vacuum chamber of the spectrometers maintained at pressures of ~$10^{-6}$ torr through a

pulsed solenoid nozzle, producing a supersonic molecular jet. Following excitation, the free induction decay (FID) signal corresponding to the relaxation of the sample is collected in the time domain. Application of a fast Fourier transform (FFT) to the FID yields frequency-domain spectra with high sensitivity and resolution, providing the experimental foundation for subsequent spectroscopic analysis.

## 3.2. Supersonic jet expansion

*Rotational cooling*

A supersonic jet expansion[1] occurs in the FTMW spectrometers due to the carrier gas, the pressure difference between the sample inlet and the chamber, and the size of the orifice that separates the two. The polyatomic molecular sample seeded into the monoatomic carrier gas undergoes collisions causing the translational and, therefore, the rotational degrees of freedom of the molecule to cool to low temperatures of ~2K. The low temperature and molecule density of the expanding gas create a free, collision-less beam of molecules. This permits the molecules to be unperturbed inside the chamber at low temperatures for a certain time period which is only limited by apparatus size.

The high pressure behind the nozzle and the small orifice (1 mm) ensures that many collisions occur as the sample passes through the nozzle. The enthalpy associated with the random motion of molecules in the nozzle is thus converted to directed mass flow as the molecules passes through the narrow orifice to reach the chamber. When gas expands through a nozzle into vacuum, it accelerates very quickly. The speed of the gas (the flow velocity) is often compared to the local speed of sound in the gas, and this ratio is called the Mach number, as defined below.

$$Classical\ speed\ of\ sound\ (a)\ = \sqrt{\frac{\gamma kT}{m}}$$

$$Mach\ number\ (M)\ = \frac{u}{a}$$

During the expansion, the mass flow velocity (u) increases and the temperature decreases as random motions are converted to directed flow causing a decrease in the local speed of sound (a) and increase in the Mach number (M). For supersonic flow, M>>1.[1]

The use of supersonic jet expansions for sample introduction offers several distinct advantages in high-resolution rotational spectroscopy. Most notably, the technique effectively eliminates common sources of spectral line broadening, including Doppler and collisional (pressure) broadening, thereby yielding transitions of exceptional sharpness and resolution. Under supersonic conditions, the population distribution is strongly biased toward the lowest rotational energy levels, which substantially simplifies the spectral patterns and facilitates the assignment of transitions. Importantly, the efficiency of this cooling is strongly influenced by the choice of carrier gas which is discussed below.

*Conformational cooling*

The variation in collisional dynamics among carrier gases has direct consequences for the conformational landscape of the molecules embedded in the beam and probed in the spectrum. When the energy barrier to interconversion between conformers is sufficiently low, higher-energy conformers may undergo relaxation to lower-energy structures during the expansion. As a result,

the recorded spectrum reflects only the most stable conformers or those corresponding to very deep minima on the potential energy surface, reducing spectral congestion and enabling more straightforward structural characterization. The extent of this conformational cooling depends not only on the barrier height but also on the carrier gas. Light gases such as helium provide faster translational cooling but less efficient internal energy transfer, whereas heavier gases such as neon or argon promote more effective vibrational and conformational relaxation due to their larger collisional cross sections and higher momentum transfer.[2] Thus, the interplay between the barrier to conformational interconversion and the thermal dynamics governed by the carrier gas composition determines the observable conformational landscape under jet-cooled conditions.

## 3.3. Chirped pulse FTMW spectrometer

The chirped-pulse Fourier transform microwave (cp-FTMW) spectrometer[3] represents a broadband alternative to the traditional narrowband Balle–Flygare design. First introduced by the Pate group at the University of Virginia around 2008,[4] the technique enables the simultaneous acquisition of several gigahertz of spectral bandwidth in a single experiment. This innovation dramatically improves the rate of data collection by several orders of magnitude compared to cavity-based methods, making it possible to survey wide frequency ranges in just a few hours or days rather than weeks. A circuit diagram is shown in figure 3.1 and is described below in detail.

The operational principle relies on the generation of a very rapid linear frequency sweep (“chirp”) by an arbitrary waveform generator, which is mixed with the output of a microwave synthesizer to create a signal centered between 8–18 GHz. The chirps on our instrument at York University span 1–3 GHz within a few microseconds, and when combined with a center frequency, allow a maximum excitation bandwidth of up to 6 GHz. This signal is amplified by a 25 W solid-state amplifier and broadcasted into the vacuum chamber through a horn antenna. A pulsed nozzle

introduces the molecular sample perpendicular to the propagation of the microwave radiation, which eliminates Doppler splitting. The strong excitation pulse polarizes molecules with rotational transitions resonant within the frequency sweep, and following the pulse, a second horn antenna collects the resulting molecular emission in the form of the decay of the molecular polarization. Because these free-induction decays (FIDs) are sometimes extremely weak, the detected signal must be amplified, filtered and averaged over $10^5$-$10^6$ cycles, depending on the molecule.

The detection system is designed to handle the full broadband emission efficiently. After initial amplification, the molecular emission is downconverted once by mixing with a second microwave synthesizer, shifting the frequency into a range suitable for direct digitization. A high-speed oscilloscope records the signal in the time domain. Fourier transformation is then applied to obtain the spectrum in the frequency domain. To ensure phase coherence across experiments, a 10 MHz rubidium clock provides a stable timing reference for all pulses. Phase-coherent averaging, either over multiple gas pulses or even within a single gas pulse by re-polarizing the same sample in rapid succession, enhances the signal-to-noise ratio.

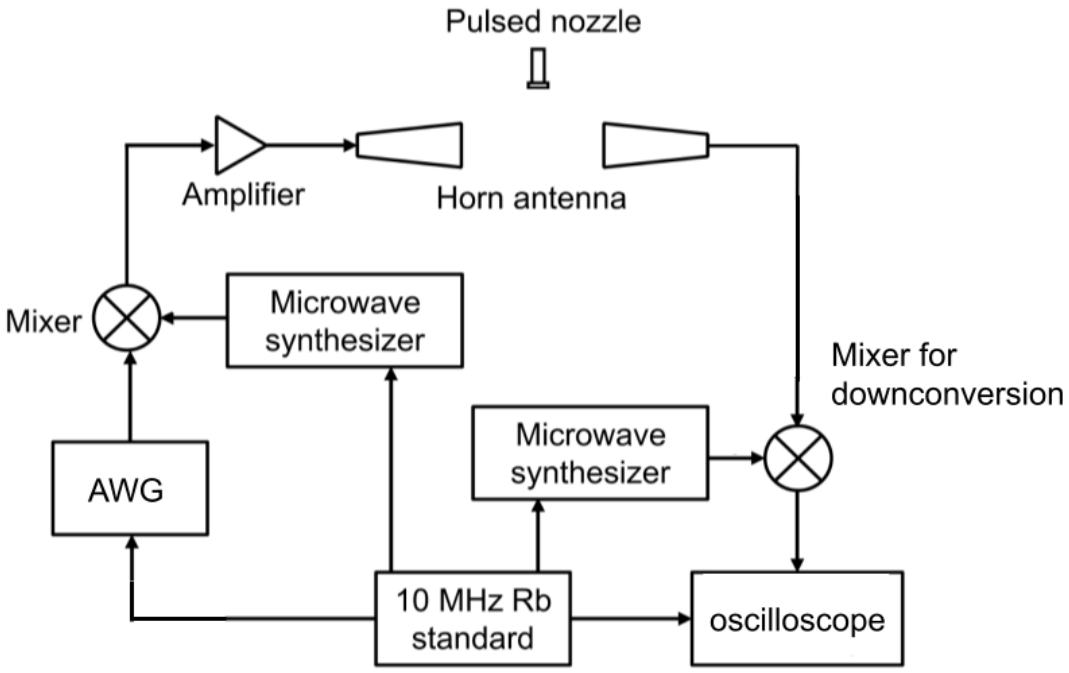


*Figure 3.1: Circuit diagram of the working of the cp-FTMW spectrometer at the van Wijngaarden lab at York University.*

The primary advantage of cp-FTMW spectroscopy over older techniques is its efficiency: spectra covering multi-gigahertz ranges can be recorded rapidly without the need to repeatedly retune a cavity, as is required for Balle–Flygare instruments. This speed, however, comes at the expense of resolution. Linewidths are ~200 kHz FWHM under conditions typically used in our laboratory, which is often insufficient to resolve structure such as internal rotation and nuclear quadrupolar splitting patterns. Nonetheless, the ability to quickly generate broadband rotational spectra makes cp-FTMW spectroscopy an invaluable tool for initial spectral surveys, conformer identification, and isotopologue detection, often serving as a powerful starting point for more refined spectroscopic investigations.

## 3.4. Balle-Flygare FTMW spectrometer

The Balle–Flygare Fourier transform microwave (FTMW) spectrometer[6] is a narrowband instrument that provides exceptionally high resolution, making it possible to resolve individual rotational transitions with linewidths on the order of a several kilohertz FWHM across a frequency range of 4–26 GHz. Its design, first introduced in the early 1980s,[7] is based on a Fabry–Pérot cavity, which forms the core of the instrument and enables efficient signal amplification and trapping of microwave radiation. The circuit diagram for this instrument can be seen in figure 3.3 and its operation is described in detail below.

The cavity is constructed from two spherical concave aluminum mirrors housed in a stainless-steel vacuum chamber maintained at pressures of ~$10^{-6}$ Torr. One mirror remains fixed, while the other is moved using a servo motor that allows the mirror separation, typically around 70 cm, to be adjusted precisely. When the spacing matches the desired microwave frequency for excitation, a standing wave is formed, enhancing the strength of the microwave field. Resonance is monitored by an L-shaped wire hook antenna placed at the center of the stationary mirror and connected to a diode detector. A second antenna, located at the center of the movable mirror, serves the dual purpose of transmitting excitation pulses and detecting molecular emission.

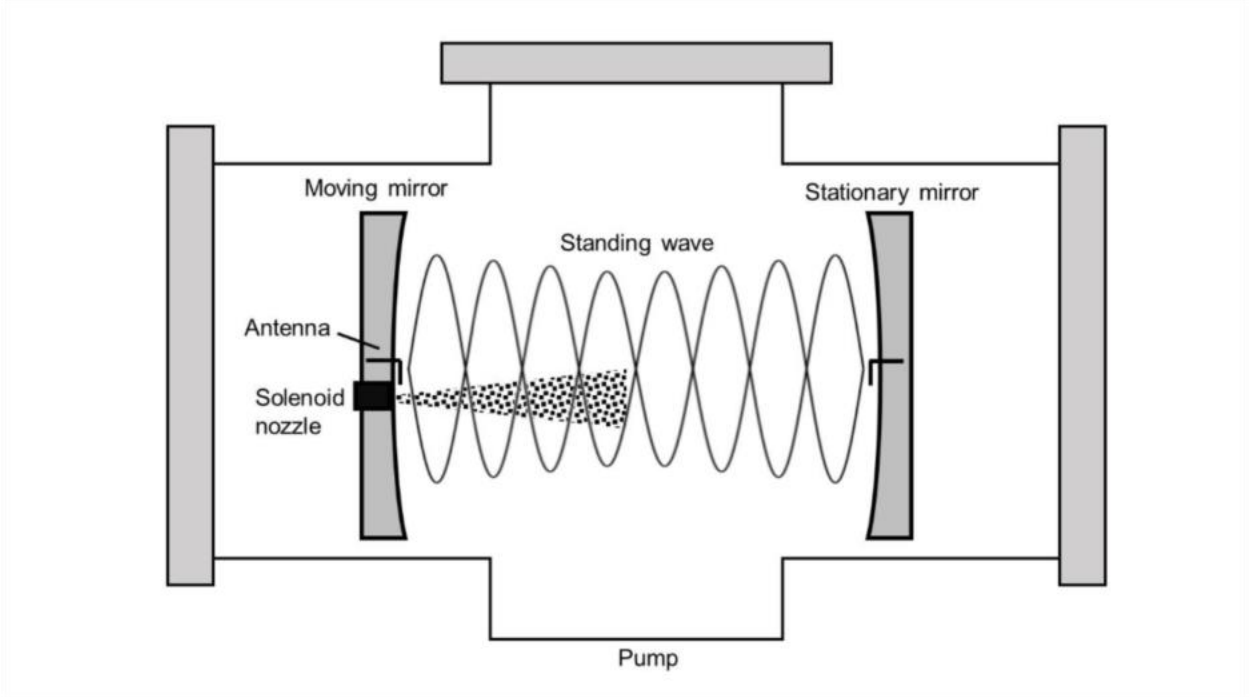


*Figure 3.2: This figure illustrates the resonating standing waves inside the chamber of the bf-FTMW spectrometer.*

Samples are delivered into the cavity via a pulsed solenoid nozzle mounted behind the movable mirror. A schematic of the cavity is shown in figure 3.2. The molecular beam is directed along the cavity axis, resulting in a Doppler doublet for each recorded rotational transition due to the coaxial alignment of the expansion and microwave field. The excitation pulse itself is generated by mixing the output of a microwave synthesizer with a 30 MHz radiofrequency signal derived from a 10 MHz reference clock. The combined signal is shaped into short pulses (up to 5 μs) using single-pole, double-throw (SPDT) switches, which also protect the sensitive detection electronics during excitation. Following the excitation pulse, the switches redirect the signal path to the detection circuit, where the weak free induction decay (FID) produced by molecular relaxation is amplified and downconverted in order to reduce the data acquisition demands.

The digitized time-domain FIDs are then Fourier transformed to yield spectra in the frequency domain. Since the signals are extremely weak, averaging over tens to thousands of experimental cycles is required to achieve adequate signal-to-noise ratios. To ensure phase coherence across averages, all timing and frequency sources—including pulse generation, delays, and digitization—are referenced to the same 10 MHz standard.

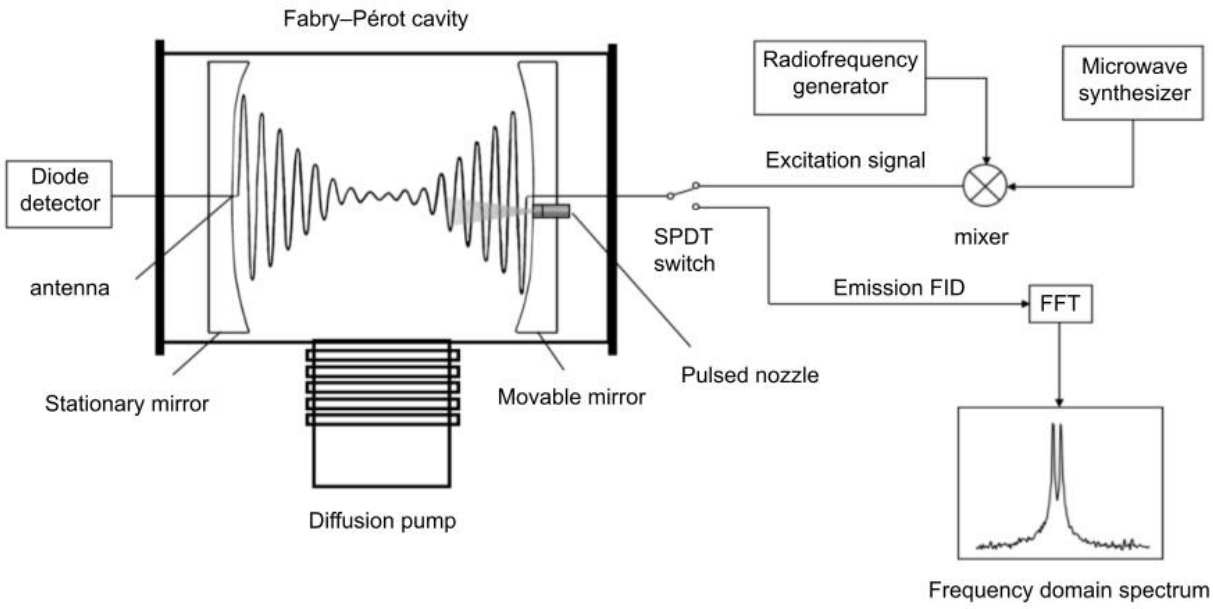


*Figure 3.3: This figure describes a simplified circuit diagram of the working of the bf-FTMW spectrometer.*

The high sensitivity achieved by the Balle–Flygare design arises from the resonant enhancement of the cavity, combined with phase-coherent averaging of repeated experiments. Under typical operating conditions, the spectrometer delivers linewidths of roughly 7 kHz (full width at half maximum) and transition frequencies that can be measured with an accuracy of about ±1 kHz.

The accuracy and precision in measurement greatly exceeds that of broadband chirped-pulse instruments and is crucial for interpreting unique spectral features, including hyperfine splittings arising from tunneling due to large-amplitude motions or the presence of nonspherical nuclei. This capability makes the Balle–Flygare FTMW spectrometer a benchmark tool for detailed structural characterization of gas-phase molecules.

In the next two chapters of this thesis, the above-described techniques and spectrometers were utilized in order to investigate the conformational preferences, dynamics and other splittings arising from the electronic environment of the molecules of interest.

## 3.5. References


1. Smalley, R. E.; Wharton, L.; Levy, D. H. Molecular Optical Spectroscopy with Supersonic Beams and Jets. Acc. Chem. Res. 1977, 10 (4), 139–145.
2. Ruoff, R. S.; Klots, T. D.; Emilsson, T.; Gutowsky, H. S. Relaxation of Conformers and Isomers in Seeded Supersonic Jets of Inert Gases. J. Chem. Phys. 1990, 93 (5), 3142–3150.
3. Evangelisti, L.; Sedo, G.; Van Wijngaarden, J. Rotational Spectrum of 1,1,1- Trifluoro-2-Butanone Using Chirped-Pulse Fourier Transform Microwave Spectroscopy. J. Phys. Chem. A 2011, 115 (5), 685–690.
4. Brown, G. G.; Dian, B. C.; Douglass, K. O.; Geyer, S. M.; Pate, B. H. The Rotational Spectrum of Epifluorohydrin Measured by Chirped-Pulse Fourier Transform Microwave Spectroscopy. *J. Mol. Spectrosc.* 2006**,** *238* (2), 200-212.
5. Brown, G. G.; Dian, B. C.; Douglass, K. O.; Geyer, S. M.; Shipman, S. T.; Pate, B. H. A 20 Broadband Fourier Transform Microwave Spectrometer Based on Chirped Pulse Excitation. Rev. Sci. Instrum. 2008, 79 (5), 53103.
6. Sedo, G.; van Wijngaarden, J. Fourier Transform Microwave Spectra of a "New" Isomer of OCS-$CO_2$. *J. Chem. Phys.* 2009**,** *131* (4), 044303.
7. Balle, T. J.; Flygare, W. H. Fabry–Perot Cavity Pulsed Fourier Transform Microwave Spectrometer with a Pulsed Nozzle Particle Source. Rev. Sci. Instrum. 1981, 52 (1), 33–45.

# Chapter 4. Allyl Phenyl Sulfide and Allyl Phenyl Ether

## 4.1. Introduction

*Chalcogens: differences in changing central atom*

Group 16 elements in the periodic table are commonly known as chalcogens. These include oxygen, sulfur, selenium, tellurium, and polonium. When a group 16 atom is covalently bonded to an organic side chain, a new subclass of compounds is created called organochalcogens. These compounds have a wide range of applications due to their unique chemical properties. For example, organosulfur compounds, such as thiols and disulfides form layered materials with sandwich-like structures, where metal atoms sandwich between two layers of S atoms by strong chemical bonds and two layers of S atoms are stacked together by weak van der Waals forces. These compounds serve as promising biosensing materials due to their excellent properties, such as large active surface areas, and suitable bandgaps.[1] The substitution of the chalcogen atom in a molecule, from a lighter one to a heavier one or vice versa, causes changes in electronegativity and polarizability of the molecule. This affects the molecular level interactions and the surface level properties of the material.[2-5] Organochalcogens also help us to understand the fundamental intramolecular interactions between chalcogen atoms and organic frameworks because the presence of lone pairs on the chalcogen atoms plays an important role in stabilizing the side chains and also affects their relative positionings.

The relevance of these compounds is further extended to materials science[6], biochemistry[7-11] and also astrochemistry. Organochalcogens could serve as molecular precursors or intermediates in the formation of complex organic molecules (COMs) in interstellar clouds and protoplanetary disks. Their presence and reactivity could contribute to the synthesis of organic compounds observed in these complex environments, shedding light on the origin of prebiotic molecules.[12-14]

*Literature*

The van Wijngaarden group has previously studied pairs of organochalcogen compounds. The main motivation behind these projects is to study the role of the central atom on directing the conformational preferences of the organic groups as a function of its size and electronic properties. We are also interested in researching how various organic side chains interact with these chalcogen atoms, and the stabilizing effects they offer. The first microwave spectroscopic study done by the group was on diallyl ether (DAE) and diallyl sulfide (DAS).[15] Quantum chemical calculations (B3LYP-D3(BJ)/aug-cc-pVTZ) revealed that the DAS has only one low energy conformer and DAE has up to twelve energy minima within 5 kJ/mol. This was confirmed by rotational spectroscopy as only the transitions corresponding to the global minimum structure of DAS were observed while DAE had a comparatively richer spectrum with transitions from nine low energy conformers. Even though these molecules differ drastically in the number of stable conformers that were observed, it was interesting to note that the arrangement of the allyl group in the lowest energy structures for both molecules was strikingly similar. This arrangement was said to be stabilized by electron donation from the lone pairs on oxygen and sulfur into the pi antibonding orbitals of the C=C of the allyl side chain. The rich conformer mixture of DAE was due to the stabilization interactions between the lone pair on oxygen and the sigma antibonding orbitals of the neighboring carbon bonds which were primarily absent in the sulfur analogue.

The uniqueness of the stable conformations due to the change from oxygen to sulfur was shown again in another study done by the group on allyl ethyl ether (AEE) and allyl ethyl sulfide (AES)[16], where quantum chemical calculations predicted fourteen low lying structures for AEE and twelve for the sulfur compound. It was experimentally observed that AES had two low energy conformers which differed in the orientations of the ethyl fragment and AEE had three structures which had distinct arrangements for the allyl group. Here, the number of unique conformations is not so different but also, the lowest energy conformations for both molecules

were exceedingly unlike. The introduction of the ethyl side chain increased the richness of the conformational equilibria of the S-bridged compound. The stability of the conformers of AEE was again attributed to the stabilizing interactions between the lone pair on oxygen and the allyl side chain and that for AES was attributed to the stabilizing interactions between the lone pair on sulfur and the ethyl fragment. The results of this study suggest that the bridging chalcogen atoms (oxygen vs sulfur) engage in unique interactions with saturated and unsaturated organic groups. Extending this to other side chains would help to test the universality of this research.

Over the last two years, the group was keen on extending this organochalcogen research to larger and more bulky side groups. We were curious to observe the similarities and differences in the conformational equilibria and the stabilizing effects between oxygen and sulfur on this new set of phenyl containing side chains to explore the impact of the bulkier organic group. In this present study, a conformational analysis was performed on allyl phenyl sulfide (APS) for the first time using quantum chemical calculations and rotational spectroscopy. A microwave study on allyl phenyl ether (APE)[17] has already been done by another research group using cp-FTMW spectroscopy. Four conformers were predicted for this ether containing compound using MP2 level of theory with a 6-311G++(3d,2p) basis set, but they experimentally observed only the two lowest energy conformations. The van Wijngaarden group has also done further work on molecules containing phenyl rings and vinyl, allyl or propargyl chains. Our former group member Manisha Kumari and current PhD student Sophia Worthington-Kirsch studied phenyl vinyl ether and sulfide, and also phenyl propargyl ether and sulfide. Hence, the observations found here are part of a bigger project being conducted by the research group.

## 4.2. Computational methods

The structure of APS consists of three dihedral angles $\alpha$, $\beta$ and $\gamma$ which can be seen in figure 4.1. Rotations about these single bonds can create various conformations.

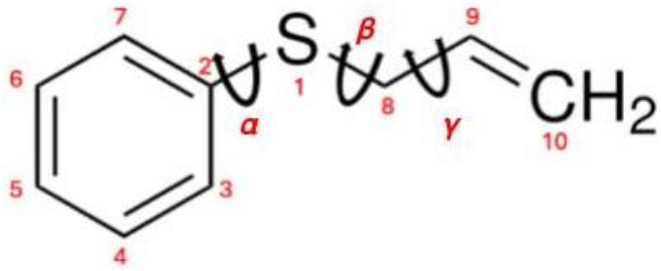


*Figure 4.1: the internal rotation about the dihedral angles of APS*

The Conformer-Rotamer Ensemble Sampling Tool (CREST)[18] was first used to carry out an automated conformer search to recognize the possible orientations. Twenty conformations were found using this automated search, out of which only 11 were unique geometries. These starting geometries were fully optimized using dispersion-corrected Density Functional Theory (DFT) B3LYP(D3)-BJ[19-21] with Dunning's aug-cc-pVTZ[22] basis set and harmonic frequency calculations confirmed the resulting structures correspond to minima. Out of these, only four unique conformers were identified within 5 kJ/mol of the lowest energy conformer and the sum of the electronic and zero-point energy (ZPE), the predicted rotational constants and the dipole moments were extracted. These can be found in table 4.1. Natural bond orbital (NBO)[23] calculations were also run using the same level of theory to gain insight into the stereo electronic effects responsible for the relative stability of the conformers. All optimizations and frequency calculations were performed using the Gaussian 16 software package.[24]

## 4.3. Experimental methods

A commercial sample of APS was purchased and used without further purification. The liquid sample of APS was seeded into the carrier gas (Ne) and introduced into the vacuum chamber of the cp-FTMW spectrometer. Here, the nozzle is placed perpendicular to the direction of the excitation pulse and hence Doppler splitting is not observed. The rotational spectrum of APS was acquired in the 8000-16000 MHz frequency range in four 2 MHz segments with 60,000 gas pulses and 25 FIDs per gas pulse resulting in 1.5 million FIDs before the FT was applied. The resulting broadband spectrum then guided the collection of high-resolution spectra and more precise frequencies using the bf-FTMW spectrometer. Again, the liquid sample of APS was seeded into the carrier gas (He) and introduced into the chamber. However, here, the nozzle is placed coaxially to the excitation pulse and hence individual lines are split due to the Doppler effect.

## 4.4. Results and Discussion

A relatively rich conformational landscape was predicted for APS after performing geometry optimization calculations. At 298 K, the predictions revealed the possibility of having 11 different conformations. The conformational space is not expected to be populated with high energy conformers in the cooled jet for the microwave spectroscopic detection. Hence, only the four conformers that possess energies that are within 5 kJ/mol of the lowest energy conformer were considered in this research. These are shown in figure 4.2 and the related energetic and spectroscopic parameters are given in table 4.1. This is similar to allyl phenyl ether[17] with 4 low energy conformers previously reported using MP2 level of theory. When optimization calculations for APE were rerun with the same level of theory used for APS (B3LYP), 5 unique conformers were predicted as represented in figure 4.3.

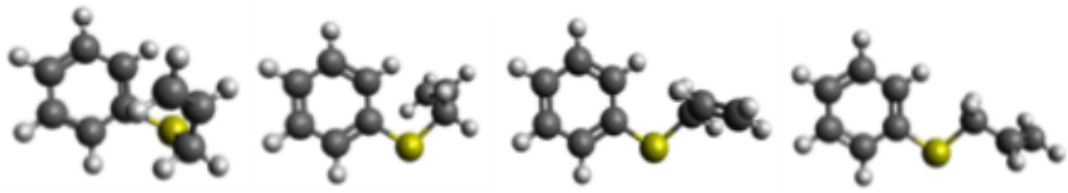

| | | | | |
|---|---|---|---|---|
| *Relative energies (kJ/mol):* | *0* | *4.05* | *5.05* | *5.23* |

*Figure 4.2: Lowest energy conformers (from left to right in increasing energetic order) of APS within 5 kJ/mol of the global minimum at the B3LYP/aug-cc-pVTZ level of theory*

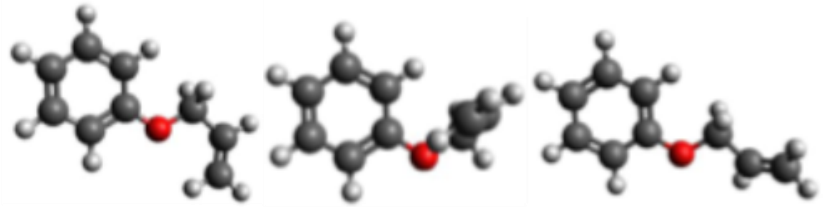

| *Relative: energies (kJ/mol)* | *0* | *0.17* | *0.64* |
|---|---|---|---|

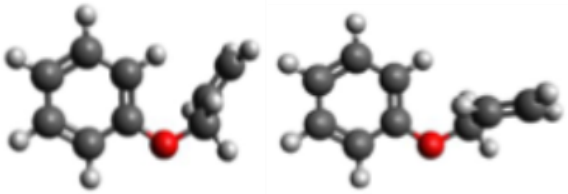

| *1.94* | *4.22* |
|---|---|

*Figure 4.3: Lowest energy conformers (from left to right in increasing energetic order) of APE within 5 kJ/mol of the global minimum at the B3LYP/aug-cc-pVTZ level of theory.*

*Table 4.1: Energetic and spectroscopic parameters for APS calculated at B3LYP-D3(BJ)/aug-cc-pVTZ level of theory*

| APS conformer | E+ZPE[1] (kJ/mol) | P%[2] | A | B | C | $\mu_a$ | $\mu_b$ | $\mu_c$ |
|---|---|---|---|---|---|---|---|---|
| 1 | 0 | 69.15 | 1847 | 837 | 727 | 0.5 | 1.3 | 0.7 |
| 2 | 4.05 | 13.46 | 2279 | 753 | 632 | 0.4 | 1.1 | 0.6 |
| 3 | 5.05 | 9.00 | 2421 | 657 | 573 | 0.2 | 1.1 | 0.3 |
| 4 | 5.23 | 8.39 | 3755 | 538 | 480 | 0.2 | 1.2 | 0.3 |

*[1] Relative total electronic + zero-point energy (ZPE)*
*[2] Boltzmann population at 298 K in %*
*A/B/C rotational constants in MHz*
*a/b/c magnitude of the electric dipole moment components in Debye*

The broadband survey spectrum of APS collected on the cp-FTMW spectrometer was compared to the predicted spectrum based on the parameters in table 4.1. The largest dipole moment for the lowest energy conformer is along the b axis at 1.3 Debye and therefore b-type transitions (where both $K_a$ and $K_c$ change by odd numbers) were the most prominent in the spectrum. Preliminary assignments of features from the lowest energy conformer were performed by identifying these unique patterns. The assigned spectrum can be seen in figure 4.4.

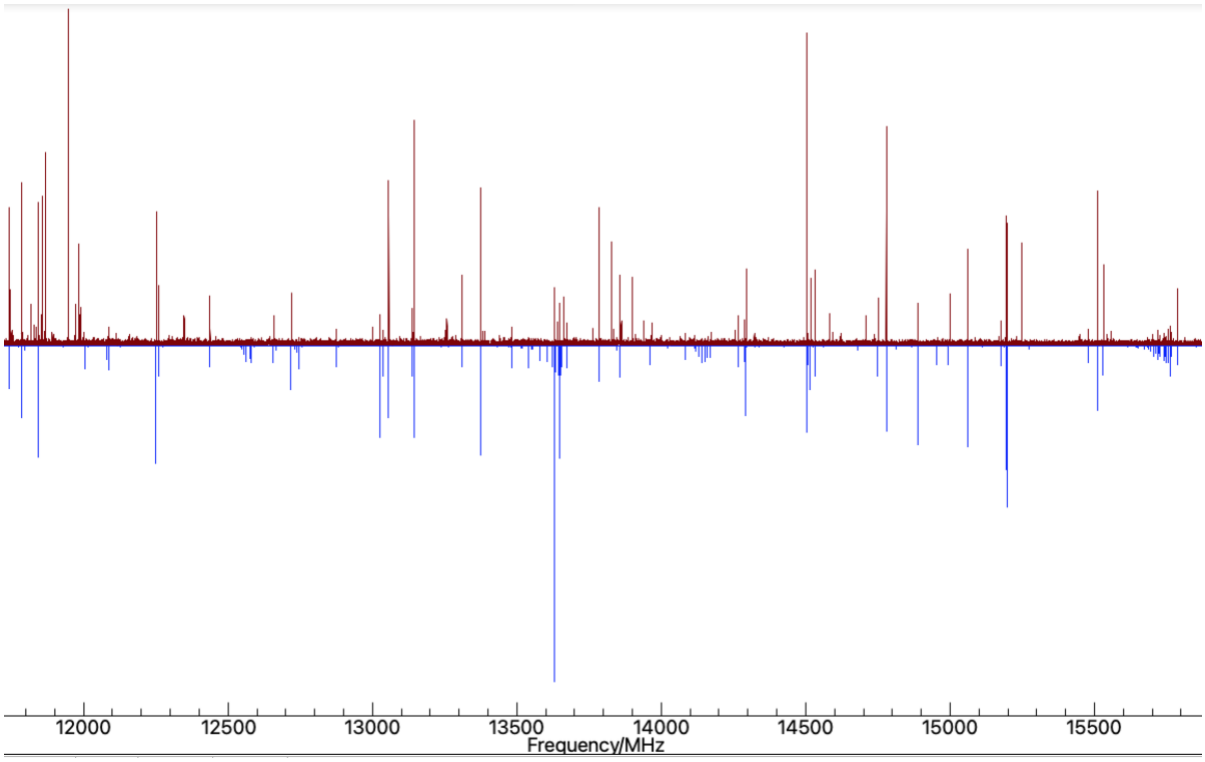


*Figure 4.4: A part of the broadband cp-FTMW spectrum (1.5 x 106 free induction decays) of APS for conformer 1. The top portion of the spectrum is the experimental spectrum, and the bottom portion is the simulated spectrum using the fitted parameters.*

This assignment was further supported by the observation of less intense c-type transitions. Unfortunately, conformer 2 and higher did not match any obvious patterns in the spectrum and were not assigned. This is likely due to the lower population and dipole moments as presented in table 4.1. The initial assignment of transitions of conformer 1 was confirmed using measurements from the bf-FTMW spectrometer, and additional transitions were recorded to extend the frequency coverage to lower ranges. A total of 115 lines were recorded, and these rotational transitions were fit using Pickett's SPFIT program[25] with Watson's A- reduced Hamiltonian[26] to determine the experimental ground state rotational constants and centrifugal distortion constants for conformer 1 of APS. The results are provided in table 4.2.

*Table 4.2: Comparison of fitted experimental and computational rotational constants and centrifugal distortion constants calculated at B3LYP-D3(BJ)/aug-cc-pVTZ level of theory*

| Parameters | Experimental results | Computational results |
|---|---|---|
| A/MHz | 1835.065818(63) | 1847 |
| B/MHz | 834.178329(40) | 837 |
| C/MHz | 731.858833(42) | 727 |
| $\Delta J$/kHz | 0.26853(35) | 0.402 |
| $\Delta K$/kHz | -1.2756(23) | -1.88 |
| $\Delta JK$/kHz | 1.5711(14) | 2.07 |
| $\delta J$/kHz | 0.02556(18) | -0.0144 |
| $\delta K$/kHz | -2.6886(66) | -0.0633 |
| $N$[1] | 115 | |
| *RMS error*/kHz[2] | 0.957 | |

[1] *N is the number of lines*
[2] *the total rms error of the least squares fit is 0.957 kHz*

Although the spectral intensity was comparatively strong only for a few lines, it was sufficient to observe transitions from singly substituted minor isotopologues in natural abundance. Since the natural abundance of $^{13}$C is ~1% and that of $^{34}$S is ~4%, the intensity of the strongest transitions for the parent were identified and then used to assign the same transitions for the minor isotopologues. There were 14 transitions assigned for $^{34}$S and 3-5 transitions assigned for each of the nine $^{13}$C isotopologues. Even though these were assigned in the survey spectrum, the transitions due to the isotopologues for conformer 1 were not observed on the bf-FTMW

spectrometer. Due to the low intensities of these transitions, the signal to noise ratio could not be optimized enough to confidently measure the lines.

A natural bond orbital (NBO) analysis was done by considering the second order perturbation energies that identify potential orbital interactions between the bridging chalcogen atom and the organic side chains that may stabilize various conformers. These calculations were carried out for the four low energy conformers of APS and five low energy conformers of APE. These calculations show the differences in lone pair (LP) characters of oxygen and sulfur. They both possess two lone pairs; LP1 of oxygen is hybridized to almost perfect $sp^2$ , with 38% 2s and 61% 2p character and the LP1 of sulfur is more like $sp^{0.5}$ with 66% 3s and 33% 3p character. This makes the LP1 of oxygen, with more p character, more directional in nature whereas the LP1 of sulfur is more isotropic and diffuse in nature. This would imply that the bridging C-O-C bond angle should be ~120° and the C-S-C bond angle, with sulfur's LP1 being less hybridized, should be smaller, nearly ~100°. This consequence was also observed, with the C-S-C bond angle being 19° smaller than the C-O-C angle.

The LP2 of both is fully p in character ($p_z$ orbital). This can also be seen in the C-S vs C-O bonding orbitals, where C-S is 85% p character whereas comparatively, the C-O bonding orbital is 70% p in character. Here, both $p_z$ orbitals are directional but due to size differences, the LP2 of oxygen has more effective overlap and LP2 of sulfur has some weak overlaps. Sulfur's 3p orbitals are larger and more diffuse than oxygen's 2p orbitals, affecting lone pair *pi* interactions. Hence, the lone pair orbitals of oxygen are able to participate in more effective overlap, and the resultant interactions are stronger than the sulfur analogue. This observation was previously noted in the groups' work on DAE and DAS where the ether analogue had more enhanced lone pair orbital interactions which were absent in DAS.[15]

There are two possible phenyl ring orientations relative to the CXC plane seen in the two low energy forms of APS and APE. It is either in the same plane as the CXC angle or a little twisted, as seen in conformer 1 of APS with a dihedral angle α of 80° adopting a near gauche conformation. The ether has a strong preference for αto be 180° adopting an anti-conformation to encourage electron delocalization from the ring's pi system to the LP2 on oxygen, as can be seen in all five of the lowest energy conformers of APE. This phenyl dihedral α, along with the values of the allyl dihedrals, $\beta$ and $\gamma$ are reported in table 4.3 and the respective figures are shown in figure 4.5 where the $\alpha$ angle is shown and conformers with similar phenyl dihedral angles are shaded in the same colour. Here, all five conformers of APE are considered alongside the first seven low energy conformers of APS for the sake of showing trends in conformational space.

*Table 4.3: The dihedral angle values for the first five conformers of APE and the first seven conformers of APS.*

| | Phenyl ($\alpha$) | Allyl 1 ($\beta$) | Allyl 2 ($\gamma$) |
|---|---|---|---|
| APE 1 | 180 | 180 | 0.0 |
| APE 2 | 172 | 83 | 0.0 |
| APE 3 | 178 | -177 | -128 |
| APE 4 | 179 | -76 | 138 |
| APE 5 | 180 | 80 | 125 |
| APS 1 | 80 | 66 | -107 |
| APS 2 | 9.0 | -79 | 2.0 |
| APS 3 | 15 | 71 | 118 |
| APS 4 | 15 | 165 | 112 |
| APS 5 | 111 | 165 | 112 |
| APS 6 | 180 | 180 | 0.0 |
| APS 7 | 80 | -179 | 0.5 |

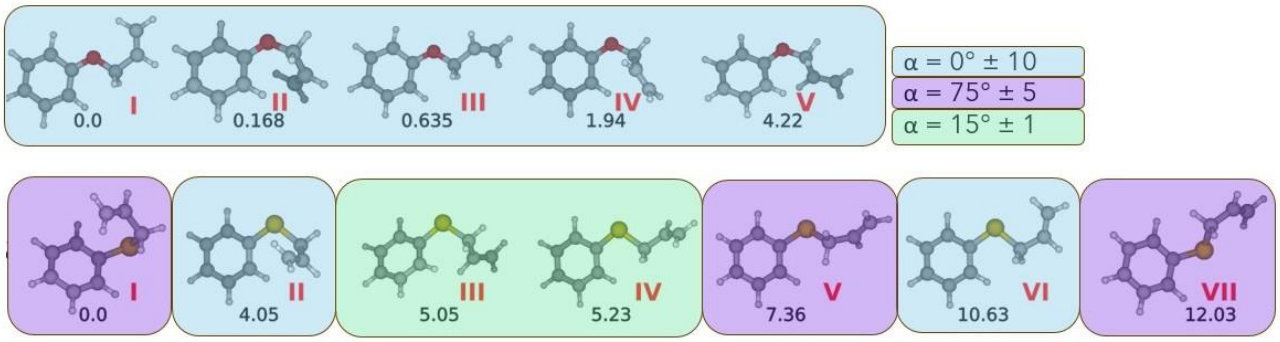


*Figure 4.5: The arrangement of the phenyl relative to the rest of the molecules for APS and APE.*

The phenyl ring orientation can be attributed to the donation of electron density from the 2p orbitals of oxygen to the pi antibonding orbitals of C2-C3 or C2-C7 of the phenyl ring. When the plane of the phenyl ring is positioned nearly perpendicular to the plane of the COC moiety, these pi antibonding interactions are significantly reduced. These interactions are also present in some conformers of APS, but the magnitude of these interactions is smaller due to the larger 3p orbital involved. Further, as the phenyl ring prefers to be twisted in the lowest energy conformers (as shown by the purple and green shading above), other interactions must be involved in stabilizing the low energy conformers.

The orientation of the allyl group in the lowest energy conformer of APS is comparable to that of the lowest energy conformer for DAS and this geometry has been observed to be stable. It is hard to pinpoint a specific reason for this geometry to be so stable for sulfides, but it is an amalgamation of various effects including steric effects due to the CSC angle being smaller than the COC angle, placing groups closer to each other. Another noteworthy cause of this could be due to the presence of donation of electron density from the LP2 (S) to the *pi** orbital of the C=C

of the allyl fragment, which was also seen in the two lowest energy forms of DAS and DAE. By comparison, in the case of APE low energy conformers, these interactions are absent.

For APE, the allyl dihedral angles of most of the low energy conformers are comparable to previously reported dihedral angles for the allyl side chain in AEE. The phenyl ring being in plane with the COC angle, essentially locked in place for all five of the lowest energy conformers, provides a substantial stabilising effect and the allyl positioning has less impact on the energy of the conformers. This flatness on the potential energy surface with respect to β and γ is the reason behind APE having a more competitive equilibrium and hence more low energy structures in a small energy window compared to that seen in APS.

Another interesting observation from this study is the fact that as seen in literature before, the ether continues to have a more competitive potential energy surface. APE has five minima within 5 kJ/mol and APS has only two. While the main driving force appears to be the high stability afforded to geometries with α of 180$^{o}$ through overlap of LP2(O) and the pi orbitals of the ring, we cannot rule out steric effects from the bulky phenyl group which depend on the chalcogen bridging angle (CXC). For the ether with its larger COC angle of 118.9$^{o}$ due to the presence of well hybridized directional bonding orbitals, the phenyl ring can orient in the COC plane with less steric repulsion than in the case of APS which has a smaller CSC angle of 99.6$^{o}$ which positions phenyl and allyl groups closer together. From table 4.3 and figure 4.5, for example, APS6 adopts a similar geometry as APE1 but lies 10.6 kJ/mol above the global minimum of the thioether conformational equilibrium.

The trends seen in this study tend to have some similarities and some differences when compared to the group's previous work, as discussed above but an important takeaway is the structural differences between the two lowest energy conformers of the ether vs the sulfide, as seen in AEE and AES. Whereas, in the DAS and DAE study, the minimum energy forms for both had very

similar geometries this present result is consistent with the results of AEE and AES where enhanced stabilising orbital interactions with different organic side chains drives the energetic ordering of both chalcogen containing species. The surprising conformational differences of APE and APS highlight that the electronic properties of the bridging chalcogen atom have a pronounced effect on the arrangement of the organic fragments. This confirms that the models of bonding, dynamics and reactivity based on carbon and its neighbours cannot be automatically deduced as one moves down the periodic table.

Overall, this was a great starter project to help understand and learn the scientific protocols behind a conformational analysis study using rotational spectroscopy. This study adds to the bigger story that our research group is trying to convey about changes in conformational structures, orientations and stabilizing factors due to changes in the central chalcogen atom from oxygen to sulfur and how they interact with various side chains.

## 4.5. Conclusion

This study has provided a detailed conformational analysis of allyl phenyl sulfide (APS) using a combination of high-resolution rotational spectroscopy and quantum chemical calculations. Geometry optimization revealed a relatively diverse conformational space, but under the conditions of the supersonic jet expansion, only the lowest-energy structure was experimentally observed. Through careful comparison of predicted spectra with broadband and cavity-based microwave measurements, conformer 1 of APS was unambiguously assigned, with 115 rotational transitions fit. The detection of isotopologues in natural abundance further reinforced the robustness of the spectral assignments, even though their low intensities limited high-resolution measurements. Together, these results provide precise experimental benchmarks for the structural

and spectroscopic properties of APS, demonstrating the complementarity between broadband survey techniques and cavity-based methods for definitive conformer characterization.

Beyond the experimental assignments, natural bond orbital (NBO) analyses offered molecular-level insight into the stabilizing interactions that govern conformer energetics. Comparisons between APS and its oxygen analogue, allyl phenyl ether (APE), highlighted how the diffuse valence orbitals of sulfur engage differently in orbital overlap compared to the more compact valence orbitals of oxygen. Furthermore, differences in phenyl ring orientation preferences between APS and APE underscore the role of central atom substitution in modulating side-chain geometry and stabilization. Collectively, these findings contribute to a broader understanding of how chalcogen substitution impacts conformational landscapes and orbital interactions between different lone pairs and a bulky phenyl group, enriching the group's ongoing efforts to unravel the structural principles that govern conformer stability and spectroscopic observability in related molecular systems.

## 4.6. References


1. Li, C.; Wang, Y.; Jiang, H.; Wang, X. Biosensors Based on Advanced Sulfur- Containing Nanomaterials. **2020**, *20* (12). https://doi.org/10.3390/s20123488.
2. S. Ye, L. Janasz, W. Zajaczkowski, J. G. Manion, A. Mondal, T. Marszalek, D. Andrienko, K. MuÃàllen, W. Pisula, and D. S. Seferos, "Self-organization and charge transport properties of selenium and tellurium analogues of polythiophene," Macromol. Rapid Commun. 40(1), 1800596 (2019).
3. E. L. Kynaston, K. J. Winchell, P. Y. Yee, J. G. Manion, A. D. Hendsbee, Y. Li, S. Huettner, S. H. Tolbert, and D. S. Seferos, "Poly(3-alkylthiophene)- block-poly(3-alkylselenophene)s: Conjugated diblock co-polymers with atypical self-assembly behavior," ACS Appl. Mater. Interfaces 11(7), 7174–7183 (2019).
4. M. Jeffries-El, B. M. Kobilka, and B. J. Hale, "Optimizing the performance of conjugated polymers in organic photovoltaic cells by traversing group 16," Macromolecules 47(21), 7253– 7271 (2014).
5. E. L. Kynaston, Y. Fang, J. G. Manion, N. K. Obhi, J. Y. Howe, D. F. Perepichka, and D. S. Seferos, "Patchy nanofibers from the thin film self-assembly of a conjugated diblock copolymer," Angew. Chem. 129(22), 6248–6252 (2017).
6. G. C. Hoover and D. S. Seferos, "Photoactivity and optical applications of organic materials containing selenium and tellurium," Chem. Sci. **10**(40), 9182–9188 (2019).
7. A. Breder and S. Ortgies, "Recent developments in sulfur- and selenium- catalyzed oxidative and isohypsic functionalization reactions of alkenes," Tetra- hedron Lett. 56(22), 2843-2852 (2015).
8. T. Nishiguchi, Y. Yoshikawa, and H. Yasui, "Anti-diabetic effect of organo- chalcogen (sulfur and selenium) zinc complexes with hydroxy-pyrone derivatives on leptin-deficient type 2 diabetes model ob/ob mice," Int. J. Mol. Sci. 18(12), 2647 (2017)

9. D. De Souza, D. O. C. Mariano, F. Nedel, E. Schultze, V. F. Campos, F. Seixas, R. S. Da Silva, T. S. Munchen, V. Ilha, L. Dornelles, A. L. Braga, J. B. T. Rocha, T. Collares, and O. E. D. Rodrigues, "New organochalcogen multitarget drug: Synthesis and antioxidant and antitumoral activities of chalcogenozidovudine derivatives," J. Med. Chem. 58(8), 3329-3339 (2015).
10. F. Penteado, B. Monti, L. Sancineto, G. Perin, R. G. Jacob, C. Santi, and E. J. LenardaÃÉo, "Ultrasound-assisted multicomponent reactions, organometallic and organochalcogen chemistry," Asian J. Org. Chem. 7(12), 2368-2385 (2018).
11. P. Oswal, A. Arora, S. Singh, D. Nautiyal, S. Kumar, G. K. Rao, and A. Kumar, "Organochalcogen ligands in catalysis of oxidation of alcohols and transfer hydrogenation," Dalton Trans. 49(36), 12503-12529 (2020)
12. Ruf, A.; Vinogradoff, V.; Duvernay, F.; Le Sergeant D'Hendecourt, L.; Danger, G.; Bouquet, A.; Mousis, O.; Boduch, P.; Schmitt-Kopplin, P.; Urso, R. G.; et al. Organosulfur Compounds Formed by Sulfur Ion Bombardment of Astrophysical Ice Analogs: Implications for Moons, Comets, and Kuiper Belt Objects. 2019, 885 (2). https://doi.org/10.3847/2041-8213/ab4e9f.
13. Fulvio, D.; Potapov, A.; He, J.; Henning, T. Astrochemical Pathways to Complex Organic and Prebiotic Molecules: Experimental Perspectives for In Situ Solid-State Studies. 2021, 11 (6), 568. https://doi.org/10.3390/life11060568.
14. Mahjoub, A.; Hodyss, R.; Choukroun, M.; Blacksberg, J.; Hand, K. P.; Altwegg, K.; Rubin, M.; HaÃànni, N.; Poston, M. J.; Ehlmann, B. L.; et al. Complex Organosulfur Molecules on Comet 67P: Evidence from the ROSINA Measurements and Insights from Laboratory Simulations. 2023, 9 (23). https://doi.org/10.1126/sciadv.adh0394.
15. Poonia, T.; Silva, W. G. D. P.; Wijngaarden, J. van. Dramatic Differences in the Conformational Equilibria of Chalcogen-Bridged Compounds: The Case of Diallyl Ether versus Diallyl Sulfide. *Physical Chemistry Chemical Physics* **2021**, *24* (1), 240–248.

16. Poonia, T.; van Wijngaarden, J. Exploring the Distinct Conformational Preferences of Allyl Ethyl Ether and Allyl Ethyl Sulfide Using Rotational Spectroscopy and Computational Chemistry. *J. Chem. Phys.* **2023**, *158* (22), 224301.
17. Grubbs, G. S.; Frank, D. S.; Obenchain, D. A.; Cooke, S. A.; Novick, S. E. The Pure Rotational Spectrum of a Claisen Rearrangement Precursor Allyl Phenyl Ether Using CP-FTMW Spectroscopy, 2016, *324*, 1–5.
18. Pracht, P.; Bohle, F.; Grimme, S.; *Automated exploration of the low-energy chemical space with fast quantum chemical methods*, *Phys. Chem. Chem. Phys.*, **2020**, *22*, 7169-7192.
19. Becke, A. D. Density-functional Thermochemistry. III. The Role of Exact Exchange. J. Chem. Phys. 1993, 98 (7), 5648–5652.
20. Grimme, S.; Antony, J.; Ehrlich, S.; Krieg, H. A Consistent and Accurate Ab Initio Parametrization of Density Functional Dispersion Correction (DFT-D) for the 94 Elements H-Pu. J. Chem. Phys. 2010, 132 (15), 154104.
21. Grimme, S.; Ehrlich, S.; Goerigk, L. Effect of the Damping Function in Dispersion 21 Corrected Density Functional Theory. J. Comput. Chem. 2011, 32 (7), 1456–1465.
22. Dunning, T. H. Gaussian Basis Sets for Use in Correlated Molecular Calculations. I. The Atoms Boron through Neon and Hydrogen. J. Chem. Phys. 1989, 90 (2), 1007–1023.
23. Weinhold, F.; Landis, C. R.; Glendening, E. D. What Is NBO Analysis and How Is It Useful? Int. Rev. Phys. Chem. 2016, 35 (3), 399–440.
24. Frisch, M. J.; Trucks, G. W.; Schlegel, H. B.; Scuseria, G. E.; Robb, M. a.; Cheeseman, J. R.; Scalmani, G.; Barone, V.; Petersson, G. a.; Nakatsuji, H.; Li, X.; Caricato, M.; Marenich, a. V.; Bloino, J.; Janesko, B. G.; Gomperts, R.; Mennucci, B.; Hratchian, H. P.; Ortiz, J. V.; Izmaylov, a. F.; Sonnenberg, J. L.; Williams; Ding, F.; Lipparini, F.; Egidi, F.; Goings, J.; Peng, B.; Petrone, A.; Henderson, T.; Ranasinghe, D.; Zakrzewski, V. G.; Gao, J.; Rega, N.; Zheng, G.; Liang, W.; Hada, M.; Ehara, M.; Toyota, K.;

Fukuda, R.; Hasegawa, J.; Ishida, M.; Nakajima, T.; Honda, Y.; Kitao, O.; Nakai, H.; Vreven, T.; Throssell, K.; Montgomery Jr., J. a.; Peralta, J. E.; Ogliaro, F.; Bearpark, M. J.; Heyd, J. J.; Brothers, E. N.; Kudin, K. N.; Staroverov, V. N.; Keith, T. a.; Kobayashi, R.; Normand, J.; Raghavachari, K.; Rendell, a. P.; Burant, J. C.; Iyengar, S. S.; Tomasi, J.; Cossi, M.; Millam, J. M.; Klene, M.; Adamo, C.; Cammi, R.; Ochterski, J. W.; Martin, R. L.; Morokuma, K.; Farkas, O.; Foresman, J. B.; Fox, D. J. Gaussian 16 Revision C.01. Gaussian Inc.: Wallingford CT 2016.

25. Pickett, H. M. The Fitting and Prediction of Vibration-Rotation Spectra with Spin Interactions. *J. Mol. Spectrosc.* **1991**, *148* (2), 371–377.
26. Watson, J. K. G. Determination of Centrifugal Distortion Coefficients of Asymmetric-Top Molecules. *J. Chem. Phys.* **1968**, *48* (10), 4517–4524.

# Chapter 5. 2-(methylthio)ethylamine

## 5.1. Introduction

This project marks the first venture by the van Wijngaarden group into the spectroscopic investigation of molecules containing sulfur, a quadrupolar nucleus ($^{14}N$), and an internal methyl rotor. Motivated by the search for prebiotic molecules of astrochemical relevance, a literature search led to a 1980 study of the Caminati group on the microwave spectra of 2-methoxyethylamine.[1] Their initial work identified a single low-energy conformer, which was later expanded in a follow-up study to include an additional conformer. This molecule was subsequently re- examined in 2018 by the Tubergen group at Kent State University, who detected two low-energy conformers in the 10–22 GHz range. Furthermore, their preliminary spectral analysis included a fit of the internal rotor tunnelling splitting, yielding experimentally determined rotational constants, internal rotation barriers (V3), and nuclear quadrupole coupling constants although their work remains unpublished. The sulfur analog is the subject of this study.

Thiols such as 2-aminoethanethiol and methyl mercaptan represent closely related systems to 2-methylthioethylamine, both in terms of chemical composition and spectroscopic behavior. These compounds feature sulfur and nitrogen containing functional groups that exhibit rich conformational and large-amplitude dynamical behavior from the terminal thiol group. The rotational spectrum of 2-aminoethanethiol, for instance, has been thoroughly investigated to characterize its conformational isomerism arising from internal rotations about the C–C and C–S bonds.[2] The presence of both an amino and a thiol group introduces the possibility of weak intramolecular hydrogen bonding and significant dipole moment changes between conformers, effects that are expected to play a similar role in alkylamino thioethers. Likewise, methyl mercaptan ($CH_3SH$) has served as a benchmark sulfur-containing molecule in rotational spectroscopy. Detailed global analyses of its torsional and vibrational states have elucidated the

coupling between internal rotation of the methyl group and overall molecular rotation.[3] Together, these studies highlight how sulfur substitution and internal rotation modulate spectral complexity depending on the barrier heights of the motions, offering valuable insight into the role of S–C and N–C linkages in more complex derivatives such as methylthioethylamines.

These findings inspired the current investigation into the sulfur analogue, 2-methylthioethylamine (2-mtea), with the aim of comparing its structural and spectroscopic features, particularly the interactions between the sulfur atom and the amine side chain and whether hydrogen bonding contributes. This project presents the first spectroscopic detection of the two lowest-energy conformers of 2-mtea. Internal rotor fitting using specialty software called XIAM[4] was performed and the experimental spectroscopic parameters including rotational constants, distortion constants, nuclear quadrupolar constants and the $V_3$ barrier was extrapolated for the two lowest energy conformers that were observed in the jet.

## 5.2. Computational methods

The structure of 2-mtea consists of three dihedral angles beta, gamma, and delta which can be seen in figure 5.1. Firstly, CREST[5] was used to carry out an automated conformer search to recognize the possible orientations. Nineteen unique conformations were found using this search. These starting geometries were fully optimized using the dispersion-corrected Density Functional Theory (DFT) B3LYP(D3)-BJ[6-8] with Dunning's aug-cc-pVTZ[9] basis set. After looking at the output files of these calculations, and carefully comparing the energies, rotational constants and dipole moments, it was found that five of these geometries were isoenergetic structures and not different minima on the potential energy surface. Hence, in total, fourteen unique conformers were predicted for 2-mtea within 11 kJ/mol of the global minimum. The sum of the electronic and zero-point energy (ZPE), the predicted rotational constants, and the dipole moments of these

conformations were extracted and are shown in table 5.1. Scans of the methyl rotor for the two lowest energy conformers were done similarly by stepping the C-S-C-H dihedral to determine the barrier to internal rotation (V3) of the $CH_3$ group using the same level of theory. These computationally predicted barriers were 6.3 kJ/mol for conformer 1 and 6.2 kJ/mol for conformer 2. These values suggest relatively low barriers to internal rotation implying that A/E splitting patterns due to $CH_3$ internal rotation is resolvable within our instrument capabilities. Natural bond orbital (NBO)[10] calculations were also run using the same level of theory to gain insight into the stereoelectronic effects responsible for the relative stability of the conformers. All calculations were performed using the Gaussian 16 software package.[11]

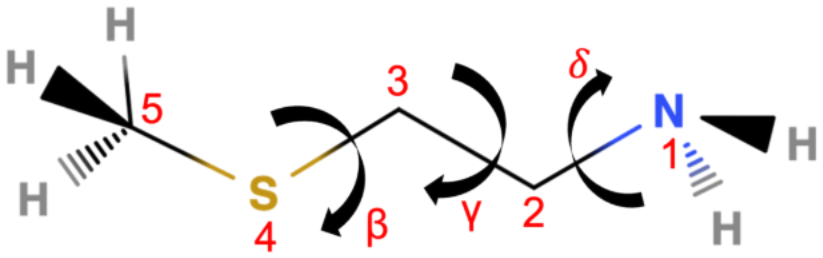


*Figure 5.1: The internal rotation around the beta, gamma and delta dihedral angles for 2-mtea.*

## 5.3. Experimental methods

A commercial sample of 2-mtea was purchased and used without further purification. The liquid sample of 2-mtea was seeded into the carrier gas (He) and introduced into the vacuum chamber of the cp-FTMW spectrometer. Here, the nozzle is placed perpendicular to the direction of the

receiving antenna and hence Doppler splitting is not observed. The rotational spectrum of 2-mtea was acquired in the 8000-16000 MHz frequency range in four 2 MHz segments with 60,000 gas pulses and 25 FIDs per gas pulse resulting in 1.5 million FIDs before the FT was applied. The first broadband spectrum consisted of many transitions that could not be assigned to any known spectral features. In order to confidently assess the issue, another cp spectrum was obtained and this time, the unassigned lines were not present. These extra transitions were, in all probability, due to contaminants in the nozzle or signals from previous molecules being studied. The resulting broadband spectrum then guided the collection of high-resolution spectra and more precise frequencies using the bf-FTMW spectrometer. Again, the liquid sample of 2-mtea was first seeded into the carrier gas (He) and introduced into the chamber. However, due to the lack of a sufficient signal to noise ratio for conformer 1, Argon was tried as a carrier gas hoping to improve the signal as it helps to populate only the lowest energy levels and most stable conformers.

## 5.4. Results and discussion

Following geometry optimization calculations, 2-mtea was found to exhibit a relatively complex conformational landscape, attributed to three rotatable dihedral angles, the presence of sulfur and nitrogen atoms, and a methyl rotor. Computational predictions revealed up to fourteen conformers, but under jet-cooled conditions, only those within 5 kJ/mol of the global minimum were considered, as higher-energy forms are unlikely to populate due to limited relaxation. Within this energy window, six unique low-energy conformers were predicted (figure 5.2), and their respective energetic and spectroscopic parameters are summarized in table 5.1.

Conformers 1 and 2, and 5 and 6 form structurally related pairs with similar ß and γ angles, closely spaced relative energies and differ only by the orientation of the $NH_2$ group (δ). Although

these pairs have very similar rotational constants, they have distinguishable spectra based on their unique dipole moments.

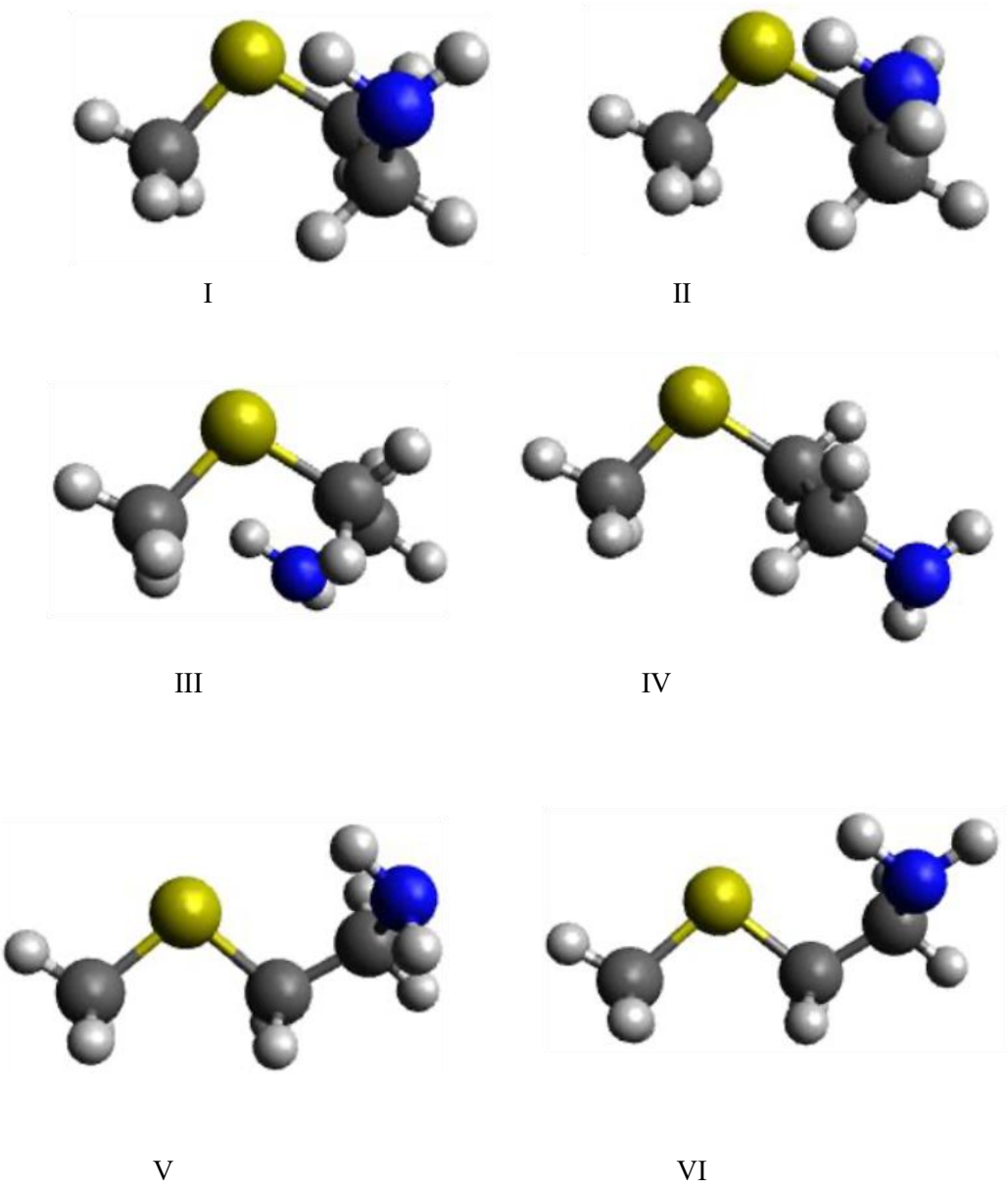


*Figure 5.2: Lowest energy conformers (from left to right in increasing energetic order) of 2-mtea within 5 kJ/mol of the global minimum at the B3LYP/aug-cc-pVTZ level of theory.*

*Table 5.1: Energetic and spectroscopic parameters for 2-mtea calculated at B3LYP-D3(BJ)/aug-cc-pVTZ level of theory*

| Conformer | [1]Relative energy (kJ/mol) | A | B | C | $\mu_a$ | $\mu_b$ | $\mu_c$ |
|---|---|---|---|---|---|---|---|
| 1 | 0 | 6695 | 2217 | 2152 | 0.4 | 0.3 | 1.3 |
| 2 | 0.517 | 6757 | 2234 | 2171 | 0.1 | 2.4 | 0.4 |
| 3 | 3.48 | 8919 | 1841 | 1660 | 0.2 | 0.6 | 1.4 |
| 4 | 3.86 | 6171 | 2554 | 2109 | 1.1 | 0.3 | 0.2 |
| 5 | 4.33 | 9493 | 1930 | 1815 | 1.3 | 1.6 | 1.3 |
| 6 | 4.52 | 9260 | 1963 | 1862 | 0.1 | 0.9 | 0.1 |
| 7 | 4.75 | 9002 | 1855 | 1669 | 1.1 | 0.9 | 0.6 |
| 8 | 5.51 | 9004 | 1840 | 1671 | 0.7 | 2.4 | 0.2 |
| 9 | 5.66 | 6164 | 2485 | 2068 | 0.5 | 0.6 | 1.7 |
| 10 | 5.81 | 12841 | 1623 | 1493 | 0.6 | 2.4 | 0.0 |
| 11 | 7.07 | 6015 | 2610 | 2033 | 2.3 | 0.5 | 1.1 |
| 12 | 7.16 | 12905 | 1640 | 1503 | 0.5 | 0.7 | 0.8 |
| 13 | 10.18 | 10257 | 1975 | 1778 | 0.8 | 2.2 | 0.6 |
| 14 | 10.82 | 5951 | 2549 | 2274 | 1.9 | 0.0 | 1.2 |

*[1] Relative total electronic + zero-point energy (ZPE)*
*A/B/C rotational constants in MHz*
*μa/μb/μc magnitude of the electric dipole moment components in Debye*

The initial broadband spectrum of 2-mtea from the cp-FTMW spectrometer was compared with theoretical spectral predictions. Notably, the simulated intensities indicated that conformer 2 should have the most intense transitions due to a higher b-axis dipole moment (2.4 D), in contrast to the largest dipole component of conformer 1, which lies along the c-axis (1.2 D). The observed survey spectrum revealed splitting of the transitions which could arise from the relatively low barriers to $CH_3$ rotation or the $^{14}N$ hyperfine splitting.

Preliminary spectral line assignments were made for conformer 2 prior to conformer 1. A portion of the assigned spectrum is presented in figure 5.3, showing the highest intensity transitions

which occurred between 13000 and 15000 MHz, predominantly consisting of Q-branch transitions ($\Delta J = 0$) of both conformers. For conformer 2, where the b-dipole component dominates, the observed transitions were primarily of b-type ($\Delta K_a$ and $\Delta K_c = 1$), with a few c-type transitions ($\Delta K_a = 1$, $\Delta K_c = 0$) also detected. As the a-axis dipole moment was negligible, no a-type transitions were seen. In contrast, conformer 1, with its dominant dipole along the c-axis, exhibited predominantly c-type transitions, with no observable a- or b-type transitions.

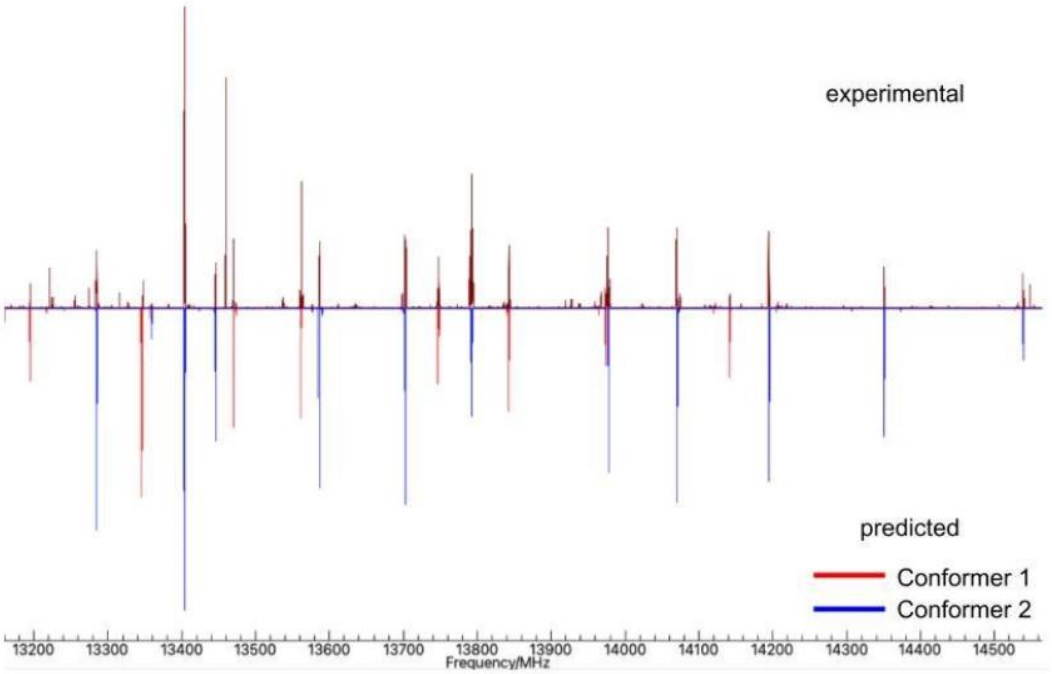


*Figure 5.3: A part of the broadband cp-FTMW spectrum (1.5 x 106 free induction decays) of 2-mtea for conformers 1 and 2. Red lines indicate conformer 1, and blue lines indicate conformer 2. The top portion of the spectrum is the experimental spectrum, and the bottom portion is the simulated spectrum.*

To confirm these assignments and better resolve the splitting patterns, high-resolution measurements were acquired using the bf-FTMW spectrometer. Due to the presence of a $^{14}N$ nucleus, nuclear quadrupole coupling introduced hyperfine splitting, which requires assigning an additional quantum number, F, representing the total angular momentum, to each $J_{KaKc}$ transition and there are typically three dominant transitions. These transitions further split into A and E torsional states due to the methyl rotor, typically producing six detectable spectral components per transition, which were also subject to Doppler splitting. A part of the bf spectrum showing the complexity in each individual transition is shown in figure 5.4. This made the measurements and fitting very laborious and complex. In general, the SPCAT software[12] reliably simulates the hyperfine splitting patterns, facilitating line assignments to their corresponding F transitions but cannot treat the methyl rotation leading to some ambiguity in the initial assignments. The internal rotor splittings can be predicted by XIAM[4] but are highly sensitive to the V3 barrier estimate and subtle changes in the geometry in terms of the alignment of the C3 axis of the CH3 group with the molecular inertial axes.

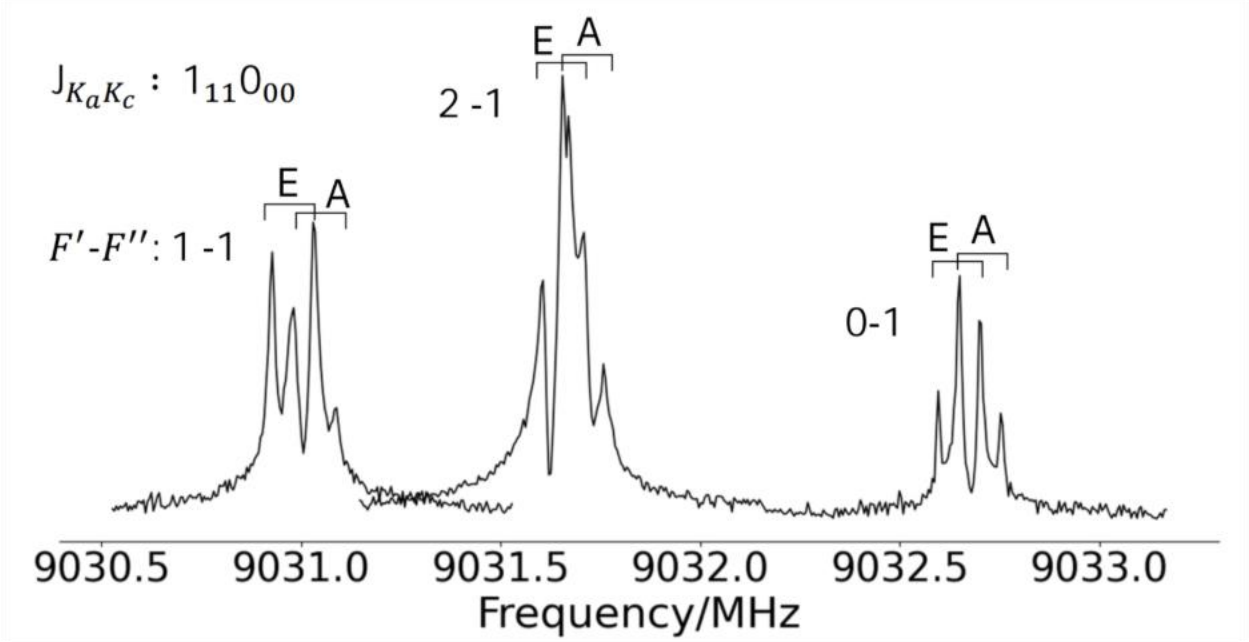


*Figure 5.4: $1_{11} - 0_{00}$ transition for conformer 2 of 2-mtea as observed on the bf-FTMW. It shows how each transition is split into multiple lines depicting different F states and A/E splitting.*

To date, approximately 100 transitions have been assigned to conformer 2 and roughly 50 to conformer 1. These frequencies were fitted using the least squares fitting program, XIAM.[4] The refined experimental spectroscopic parameters are shown in table 5.2 for conformer 1 and table 5.3 for conformer 2. It can be seen that the experimental features are in good agreement with the theoretical values, including the V3 barrier, which is 7.07 kJ/mol for both conformers, however the fit for conformer 1 has a higher rms error (or uncertainty in measurements of constants) and the V3 is only determined to one decimal place. The reason for this higher standard deviation is the lack of sufficient experimental data for conformer 1. Further attempts were made to observe additional transitions for conformer 1 by switching the carrier gas from Helium to Argon as it helps to populate only the lowest energy states, but this did not improve the signal to noise ratio by much. The spectral intensity of conformer 2 was much higher than conformer 1, and this is due to the higher dipole moment. The strongest dipole moment component for conformer 1 is

much weaker than that for conformer 2, with the populations being generally comparable (31% conformer 1 and 25% conformer 2).

*Table 5.2: Fitted spectroscopic parameters for conformer 1 of 2-mtea using XIAM. The standard deviations are given in brackets.*

| Parameters | Experimental results |
|---|---|
| A/MHz | 6755.5334 (21) |
| B/MHz | 2234.7819 (6) |
| C/MHz | 2173.0839 (7) |
| $\Delta_K$/kHz | 36.9(6) |
| $\Delta_J$/kHz | 1.9119 (fixed) |
| $\Delta_{JK}$/kHz | -8.32 (21) |
| $\delta_J$/kHz | -0.06 (7) |
| $\delta_K$/kHz | 0.02 (6) |
| $\chi_{aa}$/MHz | -0.878 (4) |
| $\chi_{bb\ -cc}$/MHz | -2.766 (6) |
| $\chi_{ab}$/MHz | -3.463 (fixed) |
| $\chi_{ac}$/MHz | -0.763 (fixed) |
| $\chi_{bc}$/MHz | 1.569 (fixed) |
| $V_3$/kJmol$^{-1}$ | 7.078 (11) |
| $F_0$/GHz | 159.29593 (fixed) |
| Delta/radians | 2.070 (4) |
| Standard deviation/kHz | 3.6 |

*Table 5.3: Fitted spectroscopic parameters for conformer 2 of 2-mtea using XIAM. The standard deviations are given in brackets.*

| Parameters | Experimental results |
|---|---|
| A/MHz | 6845.3995 (18) |
| B/MHz | 2247.9793 (4) |
| C/MHz | 2186.2018 (5) |
| $\Delta_K$/kHz | 39.3(3) |
| $\Delta_J$/kHz | 1.9221 (13) |
| $\Delta_{JK}$/kHz | -8.83 (20) |
| $\delta_J$/kHz | 0.05 (8) |
| $\delta_K$/kHz | 0.03 (6) |
| $\chi_{aa}$/MHz | 0.907 (4) |
| $\chi_{bb\ -cc}$/MHz | -3.589 (5) |
| $\chi_{ab}$/MHz | 2.215 (fixed) |
| $\chi_{ac}$/MHz | 2.292 (fixed) |
| $\chi_{bc}$/MHz | 1.374 (fixed) |
| $V_3$/kJmol$^{-1}$ | 7.075 (66) |
| $F_0$/GHz | 159.30733 (fixed) |
| Delta/radians | 2.076 (2) |
| Standard deviation/kHz | 4.6 |

Subsequent efforts were made to find higher energy conformers but without avail. A couple of transitions were observed for conformer 5, but it is hard to accurately determine whether those signals were truly from conformer 5. $^{34}$S isotopologue for conformer 2 was also tentatively assigned in the broadband cp-FTMW spectrum, but again, due to the inadequate intensity (natural abundance ~4%), it was not observed on the high-resolution bf-FTMW.

A natural bond orbital (NBO) analysis was performed by considering the second order perturbation energies that identify potential orbital interactions in order to explore the role of the

N and S heteroatoms in stabilizing the lowest energy geometries. These calculations were carried out for the six lowest energy conformers of 2-mtea. The dihedral angles, given in table 5.4, ß and γ represent <CSCC and <SCCN angles respectively as defined in figure 5.1 while δ1 and 2 represent <CCNH angles with respect to the two amine hydrogens.

*Table 5.4: The dihedral angles of the first six conformers of 2-mtea.*

| Conformer | ß | γ | δ1 | δ2 |
|---|---|---|---|---|
| 1 | 72 | 60 | 53 | 65 |
| 2 | 72 | 63 | 178 | 58 |
| 3 | 72 | 179 | 60 | 60 |
| 4 | 98 | 60 | 173 | 70 |
| 5 | 171 | 67 | 61 | 57 |
| 6 | 166 | 70 | 59 | 178 |

As mentioned above, the low energy conformers of 2-mtea can be grouped together in pairs based on structural similarities in ß and γ, rotational constants and extremely close relative energies. Despite all this, they produce unique rotational spectra due to their dipole components. These pairs can be visually seen in figure 5.5 where the pairs are in enclosed boxes.

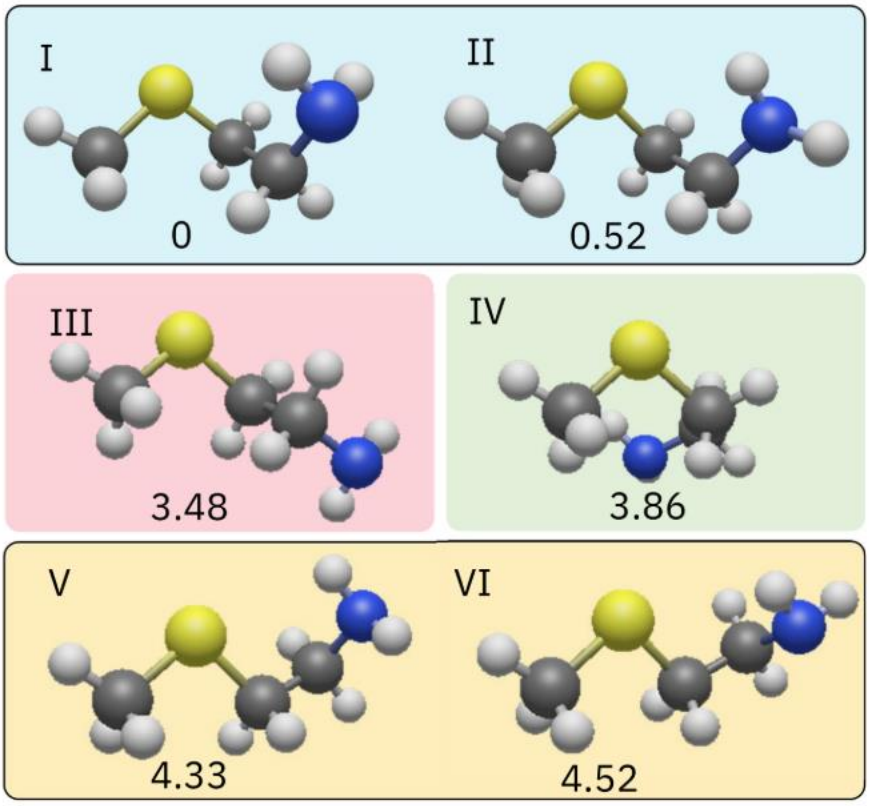


*Figure 5.5: The six lowest energy geometries of 2-mtea, with pairs of conformers in enclosed boxes and the different colors represent structural similarities based on ß and γ dihedral angles. The relative energies are given in kJ/mol.*

For the four lowest energy conformations, the near gauche (60°) ß angle was found to be stabilized by LP(S) → σ*($C_2$-$C_3$) type interactions which involve electron donation from the lone pairs on sulfur to the sigma antibonding orbitals of $C_2$-$C_3$. This is not seen in the higher energy conformers 5 and 6 where the ß angle is in a near anti (180°) orientation.

The γ angle in near gauche orientation is also preferred with five of the six lowest conformers adopting this position. This stability of γ can be attributed to improved orbital overlap between the sigma bonding orbitals of $C_2$-H and $C_3$-H with the sigma antibonding orbitals of $C_3$-S and $C_2$-N, respectively.

The different pairs of conformers, 1 and 2 and 5 and 6 (in enclosed boxes), only differ in their δ orientations. Although the heavy-atom backbone (C–C–S–N) remains nearly identical in both structures, the direction of the nitrogen lone pair and the associated N–H bond geometry produce key differences in the electronic environment. As a result, the two conformers differ in their dipole-moment components while exhibiting nearly identical rotational constants. The reorientation of the amine group changes the distribution and projection of the molecular dipole along the principal inertial axes, leading to distinct patterns of a, b, and c type transition intensities in the rotational spectrum. These differences allow the two species to be distinguished experimentally, even when their rotational constants and relative energies differ only slightly. This behavior indicates that the observed species correspond to distinct conformational minima, rather than tunneling components of a single structure caused by amine inversion. In contrast, pure amine inversion would generate tunneling doublets for each transition of a single conformer rather than unique selection rules as observed here. The spectral features observed here are most consistently explained by the presence of two low-energy conformers that differ in the amine orientation.

The lower energy partners in each pairing have their N-H bonds lying in near gauche (δ1 and δ2 both) orientations relative to the $C_2$-$C_3$ axis. This orientation of the N-H bonds positions the LP(N) to get more favourable overlap with the δ*($C_2$-$C_3$) bonds. The higher energy partner has one N-H bond (δ1 or δ2) preferring a gauche orientation and the other N-H bond preferring a near anti orientation with respect to the $C_2$-$C_3$ axis. This orientation positions the LP(N) for overlap with δ*($C_2$-H) bonds however the magnitude of this interaction is smaller than for the lower energy partner which is the reason behind these conformations being less stable than their counterparts.

This research shows strong potential for expansion into a broader class of sulfur and nitrogen containing compounds with astrochemical significance. Experimental work on a related species,

2-ethylthioethylamine (2-etea), is currently being conducted by a member of the group, Polity Chheang. The results of both these projects revealed spectroscopic parallels and dissimilarities which shows potential for further expanding this research to the methoxy analogue of 2-etea to compare the effects of chalcogen substitution on the orientation of the amine and the conformational landscape.

## 5.5. Conclusion

Rotational spectroscopic and computational analyses of 2-mtea revealed a complex conformational landscape arising from the flexibility of the C–C–S–N backbone and the orientation of the amine and methyl groups. Of the fourteen predicted minima, six low-energy conformers within 5 kJ/mol of the global minimum were identified as accessible under jet-cooled conditions. Two of these were experimentally observed and assigned through broadband and high-resolution FTMW spectroscopy, distinguished primarily by the orientation of the $NH_2$ group. Despite their nearly identical rotational constants, differences in their dipole-moment components led to distinct transition types and intensities. The experimentally fitted rotational and hyperfine parameters were in excellent agreement with theoretical predictions, including the methyl internal rotation barrier.

NBO analysis revealed that the stability of the lowest-energy conformers originates from LP(S) → σ*($C_2$–$C_3$) and LP(N) → σ*($C_2$–$C_3$) donor–acceptor interactions, which favor gauche geometries for both the sulfur and amine substituents. The two experimentally observed conformers were confirmed to be distinct minima rather than tunneling states arising from amine inversion. Overall, this work demonstrates how subtle intramolecular interactions and lone-pair effects govern conformational preferences in amine-substituted thioethers and provides a

foundation for understanding the influence of chalcogen substitution on amine orientation and molecular flexibility.

## 5.6. References


1. Caminati, W.; Dell'Erba, A.; Favero, P. G. Microwave Spectrum of 2-Methoxyethylamine. *J. Mol. Struct.* **1986**, *141*, 261– 266.
2. Nandi, R. N. *Microwave Spectral Studies of Rotational Isomerism in 2-Aminoethanethiol. J. Mol. Spectrosc.* **1982**, *95*, 1–10.
3. Zakharenko, O.; Motiyenko, R. A.; Margulès, L.; Guillemin, J. C. *Rotational Spectroscopy of Methyl Mercaptan $CH_3SH$: Global Analysis of Torsional States. Astron. Astrophys.* **2019**, *629*, A73.
4. Woods, R. A general program for the calculation of internal rotation splittings in microwave spectroscopy. J. Mol. Spectrosc. 1966, 21, 4–24.
5. Pracht, P.; Bohle, F.; Grimme, S.; *Automated exploration of the low-energy chemical space with fast quantum chemical methods*, *Phys. Chem. Chem. Phys.*, **2020**, *22*, 7169-7192
6. Becke, A. D. Density-functional Thermochemistry. III. The Role of Exact Exchange. J. Chem. Phys. 1993, 98 (7), 5648–5652.
7. Grimme, S.; Antony, J.; Ehrlich, S.; Krieg, H. A Consistent and Accurate Ab Initio Parametrization of Density Functional Dispersion Correction (DFT-D) for the 94 Elements H-Pu. J. Chem. Phys. 2010, 132 (15), 154104.
8. Grimme, S.; Ehrlich, S.; Goerigk, L. Effect of the Damping Function in Dispersion 21 Corrected Density Functional Theory. J. Comput. Chem. 2011, 32 (7), 1456–1465.
9. Dunning, T. H. Gaussian Basis Sets for Use in Correlated Molecular Calculations. I. The Atoms Boron through Neon and Hydrogen. J. Chem. Phys. 1989, 90 (2), 1007–1023.

10. Weinhold, F.; Landis, C. R.; Glendening, E. D. What Is NBO Analysis and How Is It Useful? Int. Rev. Phys. Chem. 2016, 35 (3), 399–440.
11. Frisch, M. J.; Trucks, G. W.; Schlegel, H. B.; Scuseria, G. E.; Robb, M. a.; Cheeseman, J. R.; Scalmani, G.; Barone, V.; Petersson, G. a.; Nakatsuji, H.; Li, X.; Caricato, M.; Marenich, a. V.; Bloino, J.; Janesko, B. G.; Gomperts, R.; Mennucci, B.; Hratchian, H. P.; Ortiz, J. V.; Izmaylov, a. F.; Sonnenberg, J. L.; Williams; Ding, F.; Lipparini, F.; Egidi, F.; Goings, J.; Peng, B.; Petrone, A.; Henderson, T.; Ranasinghe, D.; Zakrzewski, V. G.; Gao, J.; Rega, N.; Zheng, G.; Liang, W.; Hada, M.; Ehara, M.; Toyota, K.; Fukuda, R.; Hasegawa, J.; Ishida, M.; Nakajima, T.; Honda, Y.; Kitao, O.; Nakai, H.; Vreven, T.; Throssell, K.; Montgomery Jr., J. a.; Peralta, J. E.; Ogliaro, F.; Bearpark, M. J.; Heyd, J. J.; Brothers, E. N.; Kudin, K. N.; Staroverov, V. N.; Keith, T. a.; Kobayashi, R.; Normand, J.; Raghavachari, K.; Rendell, a. P.; Burant, J. C.; Iyengar, S. S.; Tomasi, J.; Cossi, M.; Millam, J. M.; Klene, M.; Adamo, C.; Cammi, R.; Ochterski, J. W.; Martin, R. L.; Morokuma, K.; Farkas, O.; Foresman, J. B.; Fox, D. J. Gaussian 16 Revision C.01. Gaussian Inc.: Wallingford CT 2016.
12. Pickett, H. M. The Fitting and Prediction of Vibration-Rotation Spectra with Spin Interactions. *J. Mol. Spectrosc.* **1991**, *148* (2), 371–377.

# Chapter 6. Conclusion and future work

The research carried out for this M.Sc. thesis helps to address a gap in spectroscopic knowledge of two sulfur-containing species, APS and 2-mtea, with potential for astronomical detection in the future. By exploring these species with modern rotational spectroscopic and computational methods, we have built stronger understanding of the molecular level forces that govern molecular shapes and motions.

During the course of this research, we have been able to understand the dynamics and favorable arrangements of APS compared to APE, putting emphasis on the lone pair orbitals of sulfur or oxygen and the allyl side chain and identify the various stabilizing interactions. The rotational and quartic centrifugal distortion constants for the lowest energy conformer of APS have been experimentally determined for the first time. This data enabled the identification of structural trends associated with the central chalcogen atom (either sulfur or oxygen) and the allyl side chains, which were subsequently compared to findings from previous investigations conducted by the research group on structurally related molecules.

It highlighted how the diffuse, less-hybridized valence orbitals of sulfur engage differently in orbital overlap compared to the more compact valence orbitals of oxygen. It was revealed that enhanced stabilizing orbital interactions with the two different organic side chains drive the energetic ordering of both chalcogen containing species, with the ether presenting a more competitive conformational landscape within the same energy window. This study served as an introductory project, aimed at familiarizing researchers with the methodology and analytical procedures involved in conformational analysis via rotational spectroscopy. The results contribute to a broader research initiative taken by

the van Wijngaarden group on the effects of chalcogen substitution on phenyl containing compounds.

Rotational spectroscopic analysis of 2-mtea revealed the presence of two experimentally observable low-energy conformers, distinguished primarily by the orientation of the amine hydrogens. Despite having nearly identical rotational constants and relative energies, their differing dipole-moment components produced distinct spectral signatures, confirming the existence of separate conformational minima rather than tunneling states from amine inversion. The experimental results, supported by XIAM fits and NBO analysis, demonstrated that intramolecular interactions involving the sulfur and nitrogen lone pairs stabilize gauche orientations of key dihedral angles. Overall, this study highlights how subtle electronic effects involving sulfur and nitrogen lone pairs dictate conformational stability and spectroscopic observability in flexible amino-thioethers. The close correspondence between the behaviors of 2-mtea and its ethyl analogue (2-etea) further emphasizes the systematic influence of backbone substitution on conformational diversity. Both systems highlight the influence of the sulfur atom on molecular flexibility and intramolecular interactions. Continued investigations within this molecular family, particularly comparisons with the methoxy analogue, will help elucidate the role of chalcogen substitution on amine orientation and intramolecular interactions, advancing our understanding of structure–property relationships in heteroatom-containing flexible systems.

The combined computational and experimental work on APS and 2-mtea provide detailed spectroscopic information that accurately describes the lowest energy states of these species. In addition to serving as unique fingerprints for detection in space, the knowledge gained from this thesis deepens our understanding of the intramolecular forces that govern complex conformational equilibria and can be applied to other organic chalcogens with applications extending from biology to modern materials. Future work

may focus on extending these investigations to larger or more substituted analogues to examine stabilizing intramolecular effects, explore isotopic substitution to probe tunneling phenomena, or simulate interstellar conditions to evaluate their potential astrochemical relevance, particularly as analogues of sulfur- and nitrogen-bearing species identified in space.